



2-D non-periodic homogenization to upscale elastic media for P-SV waves

Yann Capdeville, Laurent Guillot, Jean-Jacques Marigo

► To cite this version:

Yann Capdeville, Laurent Guillot, Jean-Jacques Marigo. 2-D non-periodic homogenization to upscale elastic media for P-SV waves. *Geophysical Journal International*, 2010, 182 (2), pp.903-922. 10.1111/j.1365-246X.2010.04636.x . hal-00490536

HAL Id: hal-00490536

<https://hal-polytechnique.archives-ouvertes.fr/hal-00490536>

Submitted on 8 Jun 2010

HAL is a multi-disciplinary open access archive for the deposit and dissemination of scientific research documents, whether they are published or not. The documents may come from teaching and research institutions in France or abroad, or from public or private research centers.

L'archive ouverte pluridisciplinaire **HAL**, est destinée au dépôt et à la diffusion de documents scientifiques de niveau recherche, publiés ou non, émanant des établissements d'enseignement et de recherche français ou étrangers, des laboratoires publics ou privés.



2D nonperiodic homogenization to upscale elastic media for P-SV waves

Journal:	<i>Geophysical Journal International</i>
Manuscript ID:	Draft
Manuscript Type:	Research Paper
Date Submitted by the Author:	
Complete List of Authors:	Capdeville, Yann; Institut de Physique du Globe de Paris, Dept. de Sismologie Guillot, Laurent; Institut de Physique du Globe de Paris, Équipe de sismologie Marigo, Jean-Jacques; École Polytechnique
Keywords:	Wave propagation < SEISMOLOGY, Theoretical seismology < SEISMOLOGY, Computational seismology < SEISMOLOGY, Seismic anisotropy < SEISMOLOGY, Wave scattering and diffraction < SEISMOLOGY, Numerical solutions < GEOPHYSICAL METHODS

2D nonperiodic homogenization to upscale elastic media for P-SV waves

Yann CAPDEVILLE¹, Laurent GUILLOT¹, Jean-Jacques MARIGO²

¹ *Équipe de sismologie, Institut de Physique du Globe de Paris (UMR 7154), CNRS. email: capdevil@ipgp.jussieu.fr*

² *Laboratoire de Mécanique des solides (UMR 7649), École Polytechnique*

12 January 2010

SUMMARY

The purpose of this article is to give an upscaling tool valid for the wave equation in general elastic media. The present paper is focused on P-SV wave propagation in 2D, but the methodology can be extended without any theoretical difficulty to the general 3D case. No assumption on the heterogeneity spectrum is made and the medium can show rapid variations of its elastic properties in all spatial directions. The method used is based on the two-scale homogenization expansion, but extended to the non-periodic case. The scale separation is made using a spatial low pass filter. The ratio of the filter wavelength cutoff and the minimum wavelength of the propagating wavefield defines a parameter ε_0 with which the wavefield propagating in the homogenized medium converges to the reference wavefield. In the general case, this non periodic extension of the homogenization technique is only valid up to the leading order and for the so-called first order corrector. We apply this nonperiodic homogenization procedure to two kinds of heterogeneous media: a randomly generated, highly heterogeneous medium and the marmousi2 geological model. The method is tested with the Spectral Element Method as a solver to the wave equation. Comparing computations in the homogenized media with those obtained in the original ones, shows the expected convergence with ε_0 and even better. The effects of the

2 Y. CAPDEVILLE

1 leading order correction to the source and first correction at the receivers' location are
2 shown.
3
4
5
6
7

8 1 INTRODUCTION

9
10 Seismic waves are widely used to study or image the Earth interior at all scales. In the seismological
11 or seismic exploration fields, one current challenge is to understand and take into account of, the ef-
12 fect of heterogeneities much smaller than the minimal wavelength of a wavefield propagating through
13 complex media. Indeed, geophysical elastic medium are often highly heterogeneous, at least at the
14 crust scale and lower. Nevertheless, it is well known that, in some cases at least, one can obtain quite
15 accurate ground displacement predictions when using simple propagation media, even if the real ones
16 show a high complexity in the spatial distribution of their elastic properties at smaller scale than the
17 minimum propagating wavelength. For example, very long period surface waves at the global Earth
18 scale can be modeled within a reasonable accuracy using very simple spherically symmetric elastic
19 models, and yet, the crust is highly heterogeneous at small scales. What happens is that waves nat-
20 urally “upscale” (or, equivalently, “homogenize” or “see an effective medium of”) the real medium.
21 Being able to understand in what sense a wave is upscaling a real medium is important for both the
22 imaging techniques (the inverse problem) and for waveform modeling (the forward problem). For the
23 seismic imaging inversion perspective, in order to exploit the information on the medium carried by
24 the wavefield, it is indeed of importance to understand in what sense the wavefield upscales the real
25 medium to be able to interpret the imaging results. As for the forward problem, small scale hetero-
26 geneities are a difficulty for all numerical wave equation solvers. Replacing the original discontinuous
27 and very heterogeneous medium by a smooth and more simple one, is a judicious alternative to the
28 necessary fine and difficult meshing of the original media, required by many wave equation solvers,
29 that usually leads to very high computing time.
30
31
32
33
34
35
36
37
38
39
40
41
42

43 In the geophysical community, taking into account small scales is known as finding the “effective
44 medium” of a complex medium and in the seismic community it is known as to “upscale” a medium.
45 In solid mechanics, this procedure is known as “to homogenize the medium”. In geophysics, a the-
46 oretical effort on effective medium has been going on since the sixties with some works as those of
47 Hashin & Shtrikman (1963) or Hill (1965) whose purpose was to define upper and lower bounds for
48 the effective elastic properties of heterogeneous assemblages. Other and more recent contributions to
49 this topic are described in Mainprice *et al.* (2000). For wave propagation in the seismic exploration
50 context, an important contribution was that of Backus (1962) who showed how to compute effective
51 properties for a wave propagating in finely layered media. This work is still widely used within the
52
53
54
55
56
57
58
59
60

seismic community but since then, some works have been done to obtain a more general upscaling theory (see, for example, Grechka (2003), Gold *et al.* (2000) or Tiwary *et al.* (2009) for a review of some upscaling methods used in the exploration industry). In mechanics, the method used is the so-called two scale homogenization. The latter is unfortunately often restricted to periodic media (for applications of the homogenization to the dynamic case, one may refer to Sanchez-Palencia (1980), Willis (1981), Auriault & Bonnet (1985), Moskow & Vogelius (1997), Allaire & Conca (1998), Fish & Chen (2004), Lurie (2009) or Allaire *et al.* (2009)) or dedicated to the formal mathematic foundations of the non-periodic case (e.g. Nguetseng (2003), Marchenko & Khruslov (2005)). When considering a layered medium, it is possible to extend the two scale homogenization method to the non periodic case (Capdeville & Marigo, 2007) and it can be shown that to the leading order (the homogenization theory relies on an asymptotic expansion) gives the same result as the Backus (1962) averaging technique. Nevertheless, even if the two scale homogenization solution is well know for higher dimensions problem and that it is has been applied to the elastic wave equation (e.g. Fish & Chen 2004), in practice, it is still limited to the periodic case. The challenge of our work is therefore to extend the two scale homogenization theory to the non periodic case for a spatial dimension higher than 1, for P-SV waves. The reader is encouraged to read the introductions to this topic given by Capdeville *et al.* (2010) for a 1D wave propagation, and by (Guillot *et al.*, 2010) in the case of an anti-plane elastic motion in 2D.

The wave equation solver used here is the Spectral Element Method (SEM) (see, for example, Priolo *et al.* (1994) and Komatitsch & Vilotte (1998) for the first SEM applications to the wave equation and Chaljub *et al.* (2007) for a review). This method has the advantage to be accurate for all type of waves and all type of media, as long as an hexahedral mesh, on which most of this method implementations rely, can be designed for a partition of the space. This method can be very efficient, depending on the complexity of the mesh. Nevertheless, difficulties arise when encountering some spatial patterns quite typical of the Earth like a discontinuity of material properties. In 3D realistic media, the hexahedral mesh design is often impossible.

We first introduce some concepts of spatial filtering and study wave propagation in two distinct elastic media for which computing a reference solution with SEM is a possible but difficult and time-consuming alternative. We apply two naives upscaling solution and show they are not accurate. We then develop the non-periodic homogenization for the P-SV wave propagation in 2D. We then show with examples that the method is accurate and generates wavefields that converge very well towards the reference ones (computed in the original, non-homogenized medium, with SEM).

2 PRELIMINARIES

In this preliminary section, we introduce some spatial filtering notions, we define an elastic model and suggest two trivial upscaling processes. Finally, we give examples of wave propagation in two complex models and compare the results with the one computed in the corresponding trivially upscaled models.

2.1 Spatial filtering

For any function h , we define its 2D-Fourier transform as

$$\bar{h}(\mathbf{k}) = \int_{\mathbb{R}^2} h(\mathbf{x}) e^{i\mathbf{k} \cdot \mathbf{x}} d\mathbf{x}, \quad (1)$$

where $\mathbf{x} = {}^t(x_1, x_2)$ is the position vector, $\mathbf{k} = {}^t(k_1, k_2)$ is the wave-number vector and t the transpose operator. Lets $\lambda = 1/|\mathbf{k}|$ be the associate wavelength to a wave-number vector \mathbf{k} . Our development requires to separate low from high wave-numbers of a given distribution $\bar{h}(\mathbf{k})$ around a given wave-number k_0 . For that purpose, we introduce a low-pass space filter operator which, for any function h , is defined as:

$$\mathcal{F}^{k_0}(h)(\mathbf{x}) = \int_{\mathbb{R}^2} h(\mathbf{x}') w_{k_0}(\mathbf{x} - \mathbf{x}') d\mathbf{x}', \quad (2)$$

where w_{k_0} is a wavelet, such

$$\bar{w}_{k_0}(\mathbf{k}) = \begin{cases} 1 & \text{for } |\mathbf{k}| \leq k_0; \\ 0 & \text{for } |\mathbf{k}| > k_0. \end{cases} \quad (3)$$

In practice, in order to have a wavelet w_{k_0} for which a compact support is a good approximation, we do not use such a sharp cutoff but a smooth transition from 1 to 0 around k_0 . The design of such a wavelet is detailed in appendix A and an example of such a wavelet is shown in Fig. 1.

2.2 Elastic models

In the following, we consider that, an “elastic model” in which we wish to propagate waves, is fully defined by the spatial distributions of its density $\rho(\mathbf{x})$ and elastic tensor,

$$\mathbf{c}(\mathbf{x}) = \{c_{ijkl}(\mathbf{x})\}, \quad (i, j, k, l) \in \{1, 2\}. \quad (4)$$

The elastic tensor is positive-definite and satisfies the following symmetries:

$$c_{ijkl} = c_{jikl} = c_{ijlk} = c_{klij}, \quad (5)$$

reducing the maximum number of independent parameters necessary to characterize \mathbf{c} to 6. If the model is isotropic there are only two independent parameters. Therefore, in the isotropic case, knowing

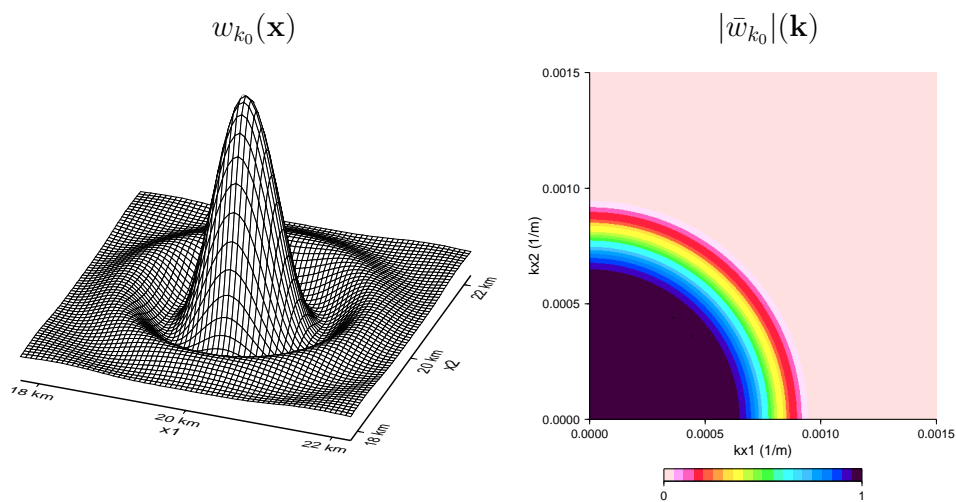


Figure 1. Wavelet example on the left and its power spectrum for positive wavenumbers on the right. The wavelet power spectrum is 1 for $|\mathbf{k}| < 6.10^{-3}m^{-1}$, 0 for $|\mathbf{k}| > 10.10^{-3}m^{-1}$ and values in-between are given by a cosine-taper (see appendix A).

the P and S wave velocities and the density, or the two Lamé elastic parameters and the density, is enough to characterize \mathbf{c} and is therefore enough to fully define an elastic model.

2.3 Naive upscaling technique based on spatial filtering

Assuming the existence of a minimum wavelength λ_m for a given wavefield propagating in a given elastic medium (ρ, \mathbf{c}) , as mentioned in the introduction, it is known by seismologists that, somehow, this wavefield is insensitive to scales much smaller than λ_m . If an original medium (ρ, \mathbf{c}) has spatial variations on scales much smaller than λ_m , there are at least two naive ways to upscale this model based on the spatial filter \mathcal{F}^{k_0} , where k_0 is a user defined wavenumber, preferentially (much) larger than $1/\lambda_m$. This wavenumber cutoff k_0 allows to define the parameter

$$\varepsilon_0 = \frac{\lambda_0}{\lambda_m}, \quad (6)$$

where $\lambda_0 = 1/k_0$, and the two naive upscaling procedures are the following ones:

- The “elastic filtering” upscaling. It is based on the low pass spatial filtering of the density and of the elastic tensor. The effective model is therefore $(\rho^{*,\varepsilon_0}, \mathbf{c}^{*,\varepsilon_0}) = (\mathcal{F}^{k_0}(\rho), \mathcal{F}^{k_0}(\mathbf{c}))$.
- The “velocity filtering” upscaling. It is based on the low pass spatial filtering of the density and of the elastic wave velocities. The model is computed from the effective density $\rho^{*,\varepsilon_0} = \mathcal{F}^{k_0}(\rho)$ and velocities $V_p^{*,\varepsilon_0} = \mathcal{F}^{k_0}(V_p)$ and $V_s^{*,\varepsilon_0} = \mathcal{F}^{k_0}(V_s)$.

At this point, a problem already appears with this low-pass filtering idea: filtering velocities or elastic parameters do not produce the same effective media for high velocities contrasts (it would in a medium

with only weak velocity contrast), therefore which one should be chosen (if any)? In the following subsection these two upscaling procedures are nevertheless tested on two elastic model examples.

2.4 Two elastic models and naive upscaling examples

In the section, we study the propagation of waves in two distinct elastic media, both of them containing heterogeneities whose size is much smaller than the minimum wavelength of the wavefield. As mentioned in the introduction, the method used to compute the reference solution and the solutions in the upscaled medium is the SEM. The mesh used to compute this reference solution match all physical discontinuities allowing a good precision but for a high numerical cost which is only possible thanks to the 2D configuration. We test here three different solutions to avoid the thin meshing of the original medium and the resulting high numerical cost:

- (i) one based on the velocity filtering upscaling ;
- (ii) one based on the elastic filtering upscaling;
- (iii) one based on a sparser mesh than the one imposed by physical interfaces but good enough to sample the wavefield . In that case, the physical discontinuities of the model are not matched by any element boundary.

Solutions (i) and (ii) are defined in the previous subsection and solution (iii) is sometimes used when the mesh design is too difficult. Komatitsch & Tromp (2002) proceeded in this way to avoid the difficult meshing of a complex Earth's crust model.

2.4.1 First example: square random model

The first model is a randomly generated 2D elastic medium. It consists of a $30 \times 30 \text{ km}^2$ square matrix of 300×300 elements of constant elastic properties surrounded by a 10 km thick strip of constant elastic properties corresponding to P and S wave velocities of 5 km s^{-1} and 3.2 km s^{-1} respectively and a density of 3000 kg m^{-3} (see Fig. 2). In each element of the matrix, the constant elastic properties and density are generated independently and randomly within $\pm 50\%$ of the outer strip elastic values and density.

The geometrical configuration of the experiment is given in Fig. 3. We compute the wave propagation induced by an explosion with a Ricker wavelet (*i.e.* second derivative of a Gaussian function) time function with a central frequency of 1.5 Hz (corresponding roughly to a corner frequency of 3.6 Hz). Ignoring the fluctuations of wave velocities in the inner square and far away enough from the source, we can estimate the minimum wavelength λ_m of the wavefield generated by the explosion to be roughly equal to 800 m . To obtain the promised accuracy of the SEM, we must generate

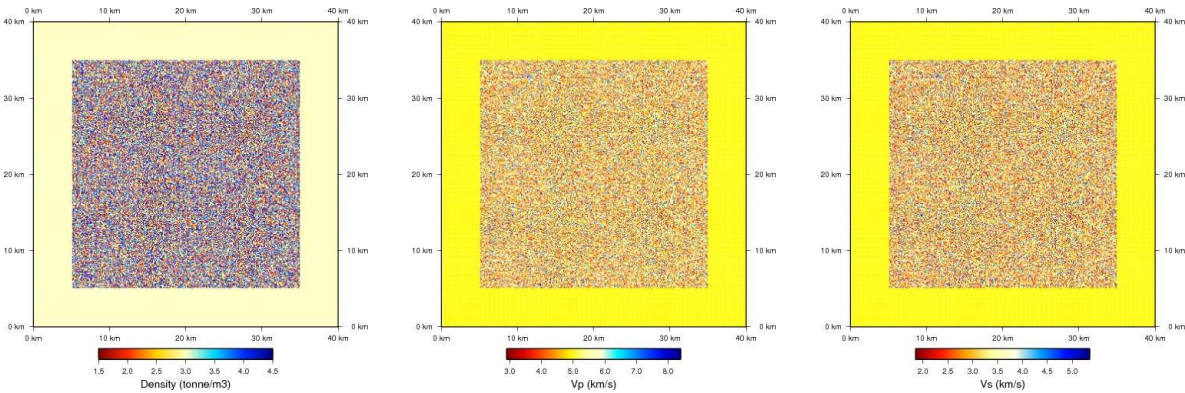


Figure 2. Square random model. Density, V_p and V_s are presented.

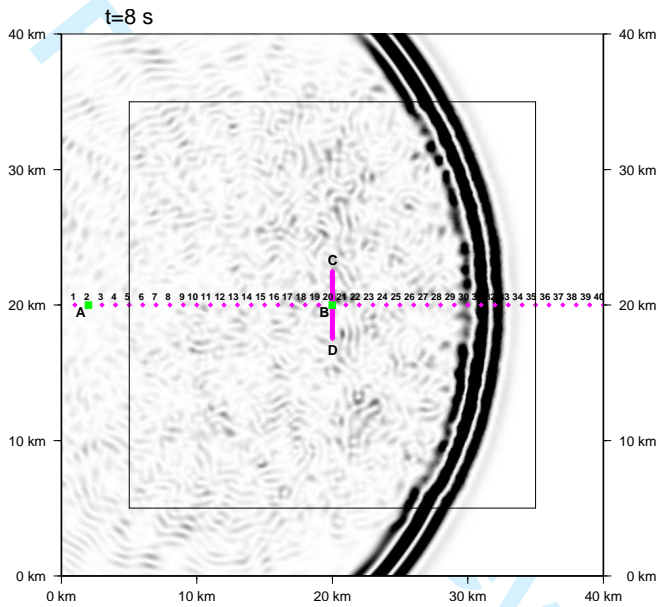


Figure 3. Configuration of the experiment for the random square model. Two source locations A and B are used (marked with green squares). Pink diamonds labeled from 1 to 40 are receiver locations and the line “CD” is a line of receivers with a 50 m vertical sampling rate. The thin black line square corresponds to the boundary of the random elastic properties area. The plotted field is a Kinetic energy snapshot at $t=8$ s for a explosion located in A with a Ricker wavelet in time of central frequency of 1.5 Hz.

a mesh based on square elements that honors all physical discontinuities of the model. In this case, the geometry is so simple that the mesh generation is trivial. Nevertheless it imposes $100 \times 100 m^2$ elements in the random matrix. Knowing that a degree 4 spectral element (a tensorial product of degree 4 polynomial basis) can roughly handle one wavelength per element, the mesh is oversampling the wavefield by a factor 8 in each direction, leading to a factor 512 in numerical cost (a factor 8 in each direction and a factor 8 in time to match the Newmark time marching scheme stability condition). For this simple 2-D case, this factor 512 can readily be handled and this allows to compute a

reference solution. Nevertheless, one can imagine that for a 3-D case, meshing the original model can quickly be out of reach for a reasonable computing power and the temptation would be high to either use a mesh that doesn't honor the physical interfaces or to simplify the model. We therefore test here the three simple solutions (i), (ii) and (iii) mentioned above. For the solution (iii), we simply use a mesh with 142×142 elements to mesh the matrix instead of 300×300 elements used to compute the reference solution. Using this sparser mesh, we are still oversampling the wavefield (by a factor 4 in each direction) but none of the physical interfaces is matched by any element boundary. We first generate a reference solution using the SEM mesh matching all interfaces. A snapshot of the kinetic energy of the wavefield generated by the source A is plotted in Fig. 3 for $t = 8$ s. In Fig. 4, we pick for instance the receiver 22 and compare waveforms obtained for the three solutions (i), (ii) and (iii) to the reference solution. It clearly appears that none of them provide a good solution, at least for standard SEM accuracy. It appears that the low-pass filtered solutions (i) and (ii) have first arrival propagating faster than in the original medium. The coda is also faster and the time delay increases with time. It is interesting to note that this time shift observed for the first arrival is consistent with the "velocity shift" observed when comparing time arrivals of waves propagating in random media compared to time arrivals computed with the corresponding average velocity (Shapiro *et al.*, 1996). Solution (iii), despite being also slightly too fast, provides a better solution for the first arrival. For coda, amplitude errors and phase time shifts can clearly be observed. Another interesting situation is shown in Fig. 5 for the same explosion as for the previous case, but located in B (see Fig. 3) at the center of the random area and recorded outside of the random area at receiver 38. On the vertical component (x_2), it can be clearly seen on the reference solution (black line) a strong ballistic S wave around $t = 8$ s which is not normally generated by an explosion located in a simple medium (as it can be seen for source A in Fig. 4). This is a S wave generated by a strong P to S wave conversion on an interface located very close to the source. All the solutions proposed in this section fail to reproduce this effect (see Fig. 5, where only the elastic filtering upscaling solution is represented (red line)).

2.4.2 Second example: the Marmousi2 model

Our second example is derived from the marmousi2 elastic model (Martin, 2004; Martin *et al.*, 2006), which is itself derived from the famous Marmousi acoustic model designed by the Institut Français du Pétrole (Versteeg, 1994). It is a 2-D geological (a section) model based upon the real geological setting from North Quenguela in the Quanza basin of Angola. The section is primarily composed of shale units with some sand and salt layers and a complex faulted area in the center of the section. From the technical point of view, 199 horizon lines are provided and each of them correspond to the top of a layer. When recombined together, it is possible to generate 435 closed objects from the horizons

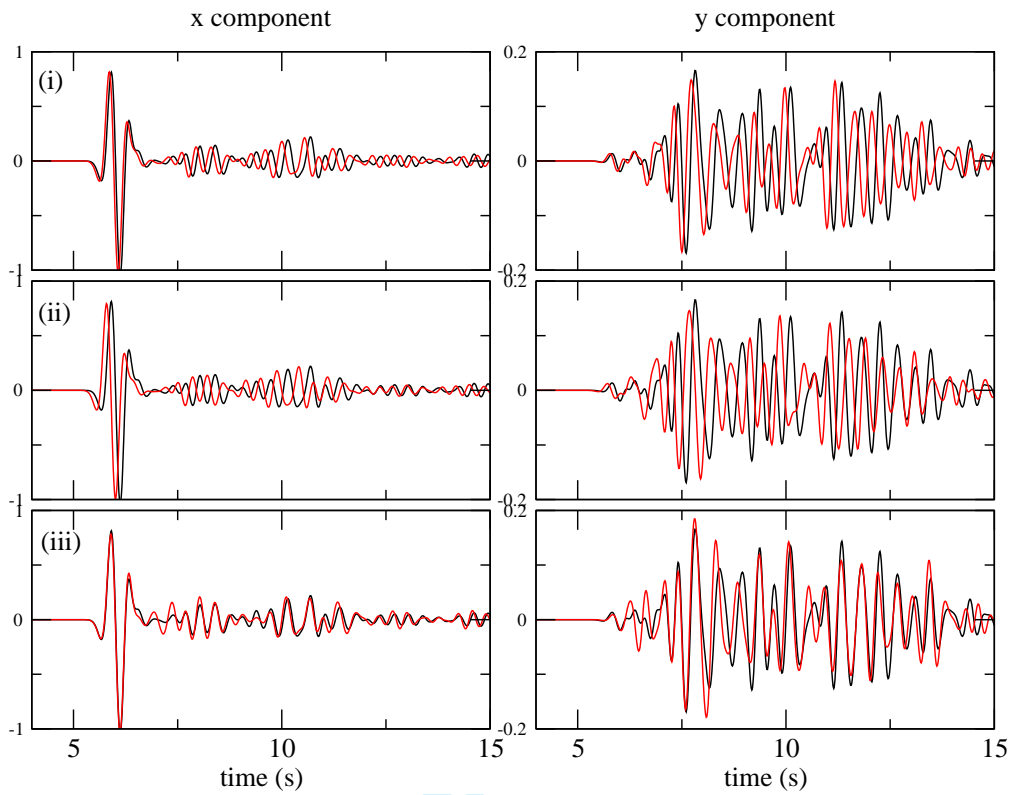


Figure 4. x_1 (left column) and x_2 (right column) components of the velocity recorded at receiver 22 for the source A (see Fig. 3). On each graph, the reference solution is plotted in black. In red, the solution obtained using solution (i) (top line of graphs), (ii) (middle line of graphs) and (iii) (bottom line of graphs).

to which constant or depth gradient elastic properties and density can be assigned. The density, P and S wave velocities are plotted in Fig. 6. For the original Marmousi and Marmousi2 models the top layer is a water layer corresponding to the ocean. We replace this layer by an elastic layer with the same P wave velocity but a non zero S wave velocity. The reason for this modification is to avoid the occurrence of a solid-fluid interface and the associated boundary layer from the point of view of homogenization which we shall present below. This case is similar to the one encountered close to a free surface (see for example Capdeville & Marigo 2008) and will be addressed in future works. We wish to pursue the same experiment as for the previous example for an explosion located at $\mathbf{x}_0 = {}^t(8\text{ km}, -100\text{ m})$ (see Fig. 8) with a Ricker time function of 6 Hz central frequency (15 Hz of corner frequency) and to do so we once again need a reference solution. Compared to the previous example, the hexahedral element mesh design is far from being trivial and leads to a complex mesh geometry and a high numerical cost. Because of the 2D configuration, some free softwares can help for its design; once the necessary closed objects are generated from the horizon lines, which is the difficult part here, we use “gmsh” (Geuzaine & Remacle, 2009), an open source mesh generator, to complete the mesh. A sample of this latter is shown in Fig. 7. Due to the large number of layers and some being

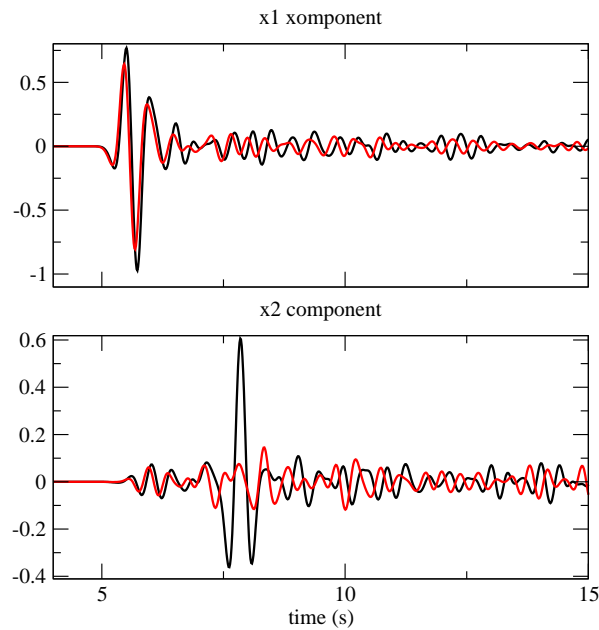


Figure 5. x_1 (top graph) and x_2 (bottom graph) components of the velocity recorded at receiver 38 for the source B (see Fig. 3). The reference solution is plotted in black. In red, the solution obtained using the elastic filtering upscaled model.

very thin (less than a meter thick), the computation is very heavy: it took seven days to compute the reference solution using 64 CPU of a recent PC cluster. This reference solution can be computed for this 2D example, but it would be impossible for a similar but 3D model. The mesh would be impossible to design and even if one manages to do so, the numerical cost would be out of reach for a of reasonable size cluster. Once again we test the three solutions (i), (ii) and (iii) proposed at the beginning of this section. For these three solutions, we use a simple regular mesh with a conforming de-refinement with depth to take advantage of the vertical velocity gradient. With such a mesh, the numerical cost is of course much chipper and it took about one hour, still with 64 CPU, to compute each of these three solutions. It is worth noting that, for such a model, because of the vertical velocity gradient, the minimum wavelength increases with depth (from $\lambda_m = 25\text{ m}$ at the top of the model to $\lambda_m = 170\text{ m}$ at the bottom). Therefore the spatial filtering we suggested previously for solutions (i) and (ii) may probably not be well adapted, and for such a case, a variable filtering with depth based on wavelet expansion would certainly be more appropriate. We nevertheless use the \mathcal{F}_0^k filtering operator with $\lambda_0 = 50\text{ m}$ (which implies $\varepsilon_0 = 2$ at the top of the model and $\varepsilon_0 = 0.3$ at the bottom). The filtering is then too harsh at the top of the model, but, because the velocity contrasts are relatively weak there, we hope it is good enough (and we will see that the homogenization procedure with the same spatial filtering parameters produces good results). The results of the computations for the three solutions are shown in Fig. 9 for the receiver location shown in Fig. 8. This location is chosen near a physical

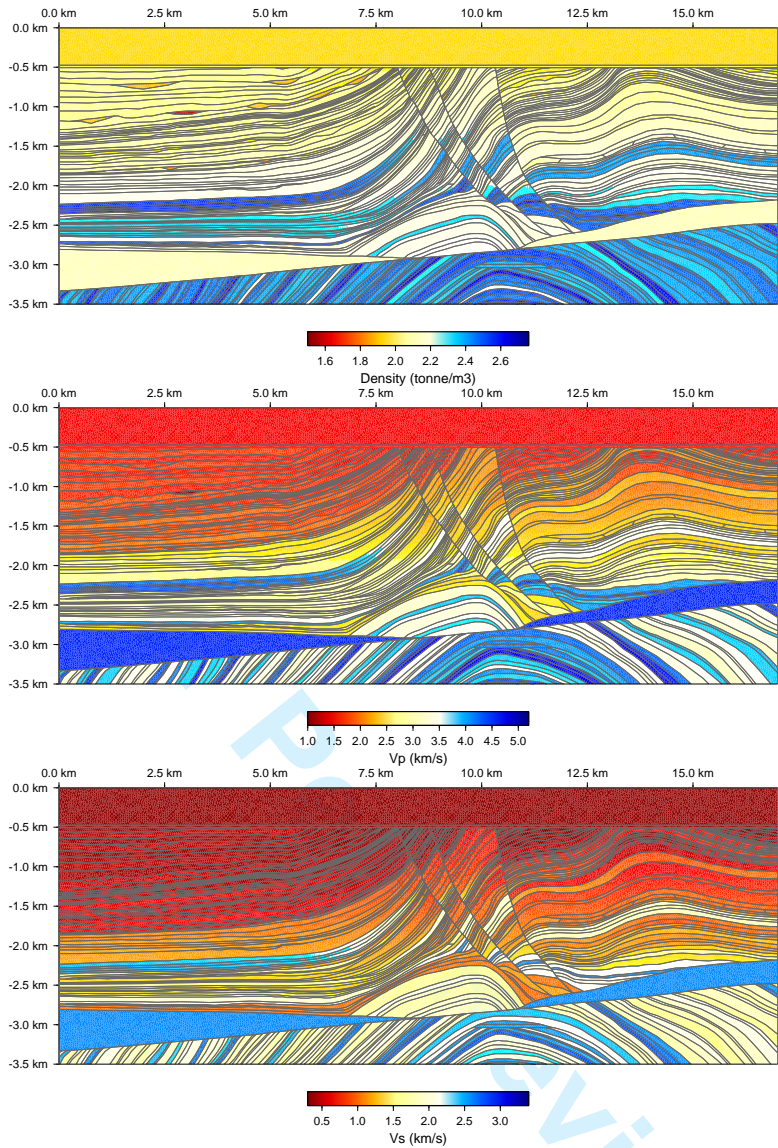


Figure 6. Marmousi2 model. Density, V_p and V_s are presented. Grey lines correspond to physical interfaces.

interface of strong velocity contrast, where the 2D effects are expected to be important. Even if this example is less spectacular than the previous one, it appears that the first arrival is faster for solutions (i) and (ii) than for the reference solution and that larger differences can be observed in the coda. The results for the solution (iii) are of better quality but some apparent misfits remain. Nevertheless, the three solutions give a better result for the marmousi model than for the square random model. The main reasons are that the propagation distance compared to the minimum wavelength is shorter in the marmousi model, and that the power spectrum of the elastic properties decreases faster with the wave number k in the marmousi model than in the square random model. Actually, for the marmousi2 model, the three solutions can provide a very good result just by decreasing ε_0 for solutions (i) and (ii), or by using a mesh that over-samples even more the wavefield for solution (iii). Nevertheless,

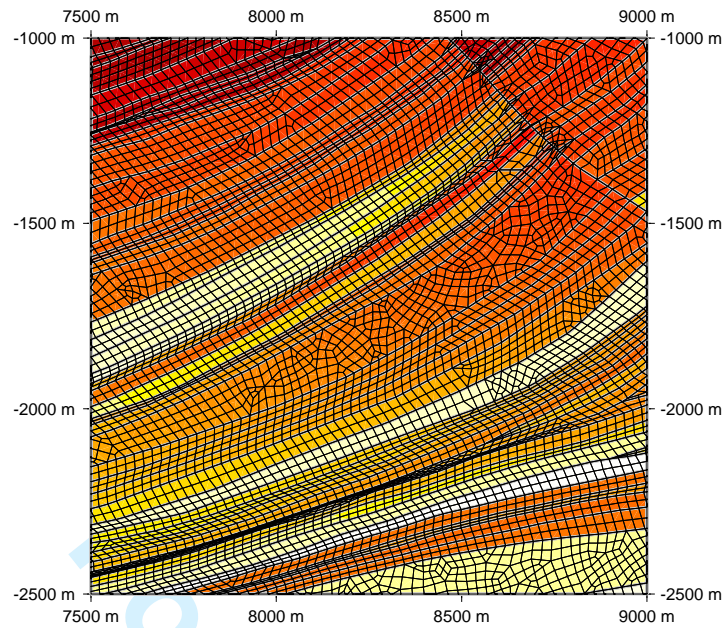


Figure 7. Sample of the spectral element mesh (black lines) used here. All physical discontinuities (grey lines) are matched by a mesh interface. The background color is the S velocity with the same color code as for Fig. 6 .

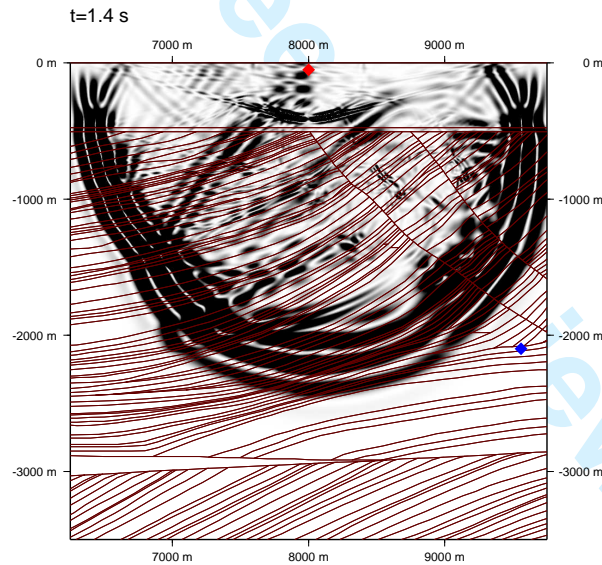


Figure 8. Kinetic energy snapshot at $t = 1.4$ s in the marmousi2 model for an explosion located at $\mathbf{x}_0 = {}^t(8\text{ km}, -100\text{ m})$ (red diamonds). The blue diamond is the receiver location used in Fig. 9 and Fig. 21.

computing these solutions is very expensive, and even in that case, depending on the model spectrum, and on the type of waves studied, there is no warranty that these solutions will converge towards the reference solution. For surface waves for example, or for interface waves in general, none of these solutions would provide an accurate result (Capdeville & Marigo, 2008).

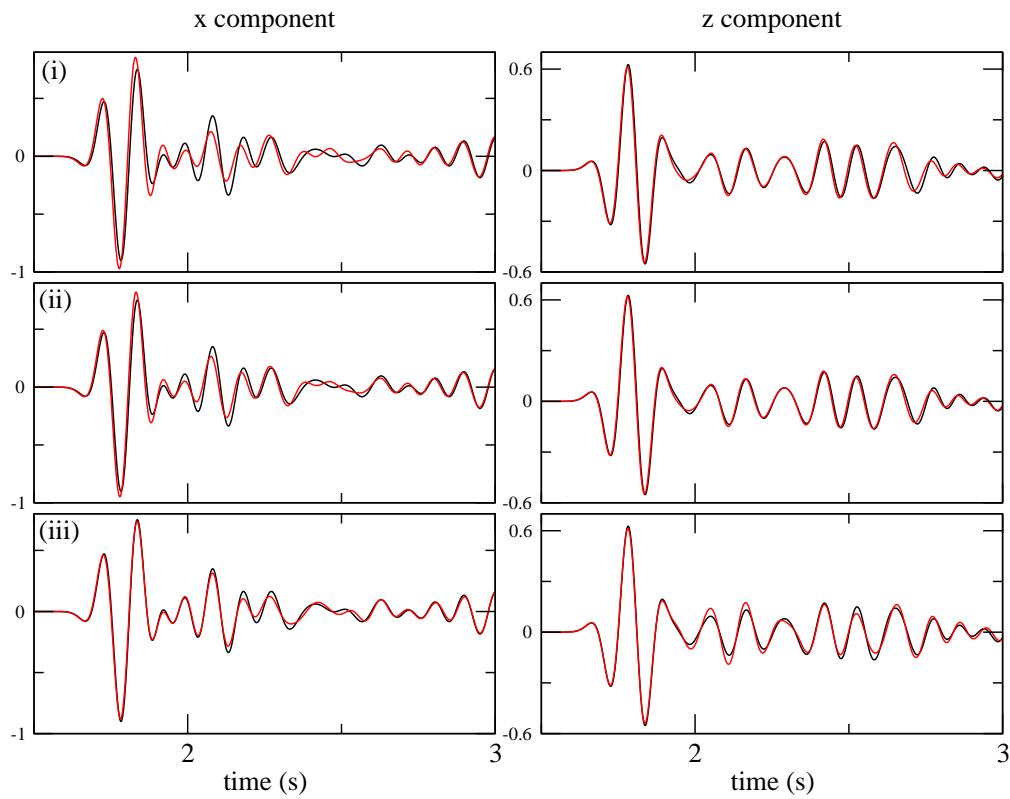


Figure 9. x (left column) and z (right column) component of the velocity recorded at receiver shown in Fig. 8. For all graphs, the reference solution is plotted in black. In red is plotted the solution obtained using solution (i) (top line of graphs), (ii) (middle line of graphs) and (iii) (bottom line of graphs).

3 THEORETICAL DEVELOPMENT

3.1 Notations

Let us first define some notations that will be used in this section. For any 4th-order tensor \mathbf{A} and second order tensor \mathbf{b} , we note

$$[\mathbf{A} : \mathbf{b}]_{ij} = A_{ijkl}b_{kl}, \quad (7)$$

where the sum over repeated subscripts is assumed. For any 4th-order tensors \mathbf{A} and \mathbf{B} , we note

$$[\mathbf{A} : \mathbf{B}]_{ijkl} = A_{ijmn}B_{mnkl}. \quad (8)$$

We will use the following compact notation for partial derivatives with respect to any variable x of a given function g :

$$\partial_x g \equiv \frac{\partial g}{\partial x}. \quad (9)$$

Finally, we will sometimes use the classical notation for time partial derivative: for any u

$$\dot{u} \equiv \frac{\partial u}{\partial t}. \quad (10)$$

3.2 Problem set up

We consider an infinite elastic plane characterized by the distributions of density $\rho^0(\mathbf{x})$, and elastic tensor $\mathbf{c}^0(\mathbf{x})$. The plane is considered as infinite in order to avoid the treatment of any boundary condition that normally would be necessary in the following development. The boundary condition problem associated with homogenization has nevertheless been addressed by Capdeville & Marigo (2007) and Capdeville & Marigo (2008) for layered media, and will be the purpose of future works for a more general case. No assumption on the spatial variability of $\rho^0(\mathbf{x})$ and $\mathbf{c}^0(\mathbf{x})$ is made, which implies that they can vary at any scale and in any direction. The plane is submitted to an external source force $\mathbf{f} = \mathbf{f}(x, t)$ and we wish to study the displacement $\mathbf{u}(\mathbf{x}, t) = {}^t(u_1, u_2)(\mathbf{x}, t)$ associated to the wave propagating in the plane. We assume that $\mathbf{f}(\mathbf{x}, t)$ has a corner frequency f_c which allows to assume that, in the far field, it exists a minimum wavelength λ_m to the wavefield \mathbf{u} . The displacement \mathbf{u} is driven by the wave equation,

$$\rho^0 \partial_{tt} \mathbf{u} - \nabla \cdot \boldsymbol{\sigma} = \mathbf{f}, \quad (11)$$

associated to the following constitutive relation between the stress $\boldsymbol{\sigma}$ and the strain $\boldsymbol{\epsilon}(\mathbf{u}) = \frac{1}{2}(\nabla \mathbf{u} + {}^t \nabla \mathbf{u})$ tensors:

$$\boldsymbol{\sigma} = \mathbf{c}^0 : \boldsymbol{\epsilon}(\mathbf{u}). \quad (12)$$

The initial conditions at $t = 0$ are assumed to be zero and radiation boundary conditions at the infinity are assumed (actually modeled using Perfectly Matched Layers version of Festa *et al.* 2005).

3.3 Homogenization problem set up

To solve the so-called two-scale homogenization problems, a small parameter ε is classically introduced :

$$\varepsilon = \frac{\lambda}{\lambda_m}, \quad (13)$$

where λ is a spatial wavelength or a scale. For a periodic medium, λ would be the length defining the periodicity of the model. In the non periodic case, another parameter is required

$$\varepsilon_0 = \frac{\lambda_0}{\lambda_m}, \quad (14)$$

where λ_0 is the user defined scale below which a wavelength is considered as belonging to the small scale (microscopic) domain. Reciprocally, wavelength larger than λ_0 is considered as belonging to the large scale (macroscopic) domain. The parameter λ_0 is user defined, but it makes sense to assume that the wavefield does interact with heterogeneities whose scales are smaller than λ_m . Therefore, choosing an $\varepsilon_0 \ll 1$, which means considering as microscopic, heterogeneities whose size is much smaller than the minimum wavelength, is probably a good guess.

In order to explicitly take microscopic scale heterogeneities into account, a fast space variable is introduced:

$$\mathbf{y} = \frac{\mathbf{x}}{\varepsilon}. \quad (15)$$

\mathbf{y} is the microscopic variable and \mathbf{x} is the macroscopic one. When $\varepsilon \rightarrow 0$, any change in \mathbf{y} induces a very small change in \mathbf{x} . This leads to the separation of scales: **\mathbf{y} and \mathbf{x} are treated as independent variables**. This hypothesis implies that partial derivatives with respect to \mathbf{x} become:

$$\nabla_{\mathbf{x}} \rightarrow \nabla_{\mathbf{x}} + \frac{1}{\varepsilon} \nabla_{\mathbf{y}}, \quad (16)$$

where $\nabla_{\mathbf{x}} = {}^t(\partial_{x_1}, \partial_{x_2})$ and $\nabla_{\mathbf{y}} = {}^t(\partial_{y_1}, \partial_{y_2})$.

We define the wavelet $w_m(\mathbf{y}) = w_{k_m}(\mathbf{y})$ where w_{k_m} is the low pass filter wavelet defined in (3) or in appendix A and $k_m = 1/\lambda_m$. We assume that the support of w_m in the space domain is contained in $[-\alpha\lambda_m, +\alpha\lambda_m]^2$ where α is a positive number that depends upon the specific design of w (see appendix A for details).

Let $\mathbf{Y}_0 = [-\beta\lambda_m, \beta\lambda_m]^2$ be a square of \mathbb{R}^2 where β is a positive number larger than α and $\mathbf{Y}_{\mathbf{x}}$ the same square but translated by a vector \mathbf{x}/ε_0 . We define $\mathcal{T} = \{h(\mathbf{x}, \mathbf{y}) : \mathbb{R}^4 \rightarrow \mathbb{R}, \mathbf{Y}_0\text{-periodic in } \mathbf{y}\}$ the set of functions defined in \mathbf{y} on \mathbf{Y}_0 and extended to \mathbb{R}^2 by periodicity. We define the filtering operator, for any function $h \in \mathcal{T}$:

$$\mathcal{F}(h)(\mathbf{x}, \mathbf{y}) = \int_{\mathbb{R}^2} h(\mathbf{x}, \mathbf{y}') w_m(\mathbf{y} - \mathbf{y}') d\mathbf{y}'. \quad (17)$$

Finally let \mathcal{V} be the set of functions $h(\mathbf{x}, \mathbf{y})$ such that, for a given \mathbf{x} , the \mathbf{y} part of h is periodic and contains only spatial frequency higher than k_m , plus a constant value in \mathbf{y} :

$$\mathcal{V} = \{h \in \mathcal{T} / \mathcal{F}(h)(\mathbf{x}, \mathbf{y}) = \langle h \rangle(\mathbf{x})\}, \quad (18)$$

where

$$\langle h \rangle(\mathbf{x}) = \frac{1}{|\mathbf{Y}_0|} \int_{\mathbf{Y}_0} h(\mathbf{x}, \mathbf{y}) d\mathbf{y}, \quad (19)$$

is still the \mathbf{y} average of $h(\mathbf{x}, \mathbf{y})$ over the periodic cell.

In this section and the next one, we proceed in the same way as in Capdeville *et al.* (2010) and

Guillot *et al.* (2010). We first assume that we have been able to define $(\rho^{\varepsilon_0}(\mathbf{x}, \mathbf{y}), \mathbf{c}^{\varepsilon_0}(\mathbf{x}, \mathbf{y}))$ in \mathcal{T} with the conditions

$$\begin{aligned}\rho^{\varepsilon_0}(\mathbf{x}, \mathbf{x}/\varepsilon_0) &= \rho^0(\mathbf{x}) \\ \mathbf{c}^{\varepsilon_0}(\mathbf{x}, \mathbf{x}/\varepsilon_0) &= \mathbf{c}^0(\mathbf{x})\end{aligned}\quad (20)$$

that set up a sequence of models indexed by ε

$$\begin{aligned}\rho^{\varepsilon_0, \varepsilon}(\mathbf{x}) &\equiv \rho^{\varepsilon_0}(\mathbf{x}, \frac{\mathbf{x}}{\varepsilon}), \\ \mathbf{c}^{\varepsilon_0, \varepsilon}(\mathbf{x}) &\equiv \mathbf{c}^{\varepsilon_0}(\mathbf{x}, \frac{\mathbf{x}}{\varepsilon}),\end{aligned}\quad (21)$$

and that, with such a set of parameters, a solution to the problem described below exists. This assumption is by far not obvious and the construction of such a $(\rho^{\varepsilon_0}(\mathbf{x}, \mathbf{y}), \mathbf{c}^{\varepsilon_0}(\mathbf{x}, \mathbf{y}))$ from $(\rho^0(\mathbf{x}), \mathbf{c}^0(\mathbf{x}))$, which is the critical point of this article, is left for section 3.5.

We look for the solutions of the following wave equation and constitutive relation

$$\begin{aligned}\rho^{\varepsilon_0, \varepsilon} \partial_{tt} \mathbf{u}^{\varepsilon_0, \varepsilon} - \nabla \cdot \boldsymbol{\sigma}^{\varepsilon_0, \varepsilon} &= \mathbf{f}, \\ \boldsymbol{\sigma}^{\varepsilon_0, \varepsilon} &= \mathbf{c}^{\varepsilon_0, \varepsilon} : \boldsymbol{\epsilon}(\mathbf{u}^{\varepsilon_0, \varepsilon}),\end{aligned}\quad (22)$$

where $\boldsymbol{\epsilon}(\mathbf{u}^{\varepsilon_0, \varepsilon}) = \frac{1}{2}(\nabla \mathbf{u}^{\varepsilon_0, \varepsilon} + {}^t \nabla \mathbf{u}^{\varepsilon_0, \varepsilon})$. The initial conditions at $t = 0$ are assumed to be zero and radiation boundary conditions at the infinity are assumed. To solve this problem, the fast space variable \mathbf{y} , defined by (15), is used. In the limit $\varepsilon \rightarrow 0$, \mathbf{x} and \mathbf{y} are treated as independent variables, implying the transformation (16), or similarly, with strain operators:

$$\boldsymbol{\epsilon}(\mathbf{u}) \rightarrow \boldsymbol{\epsilon}_x(\mathbf{u}) + \frac{1}{\varepsilon} \boldsymbol{\epsilon}_y(\mathbf{u}), \quad (23)$$

where $\boldsymbol{\epsilon}_x(\mathbf{u}) = \frac{1}{2}(\nabla_x \mathbf{u} + {}^t \nabla_x \mathbf{u})$ and $\boldsymbol{\epsilon}_y(\mathbf{u}) = \frac{1}{2}(\nabla_y \mathbf{u} + {}^t \nabla_y \mathbf{u})$.

The solution to the wave equations (22) is then sought as an asymptotic expansion in ε with $\mathbf{u}^{\varepsilon_0, i}$ and $\boldsymbol{\sigma}^{\varepsilon_0, i}$ in \mathcal{V} :

$$\begin{aligned}\mathbf{u}^{\varepsilon_0, \varepsilon}(\mathbf{x}, t) &= \sum_{i=0}^{\infty} \varepsilon^i \mathbf{u}^{\varepsilon_0, i}(\mathbf{x}, \mathbf{x}/\varepsilon, t) = \sum_{i=0}^{\infty} \varepsilon^i \mathbf{u}^{\varepsilon_0, i}(\mathbf{x}, \mathbf{y}, t), \\ \boldsymbol{\sigma}^{\varepsilon_0, \varepsilon}(\mathbf{x}, t) &= \sum_{i=-1}^{\infty} \varepsilon^i \boldsymbol{\sigma}^{\varepsilon_0, i}(\mathbf{x}, \mathbf{x}/\varepsilon, t) = \sum_{i=-1}^{\infty} \varepsilon^i \boldsymbol{\sigma}^{\varepsilon_0, i}(\mathbf{x}, \mathbf{y}, t).\end{aligned}\quad (24)$$

Note that the condition for $\mathbf{u}^{\varepsilon_0, i}$ and $\boldsymbol{\sigma}^{\varepsilon_0, i}$ to be in \mathcal{V} is a strong condition which mainly means that slow variations only in \mathbf{x} and fast variations only in \mathbf{y} are required. It is the equivalent to the \mathbf{y} periodic condition in the periodic case. Introducing the expansions (24) in the wave equations (22) and using (23) we obtain:

$$\rho^{\varepsilon_0} \partial_{tt} \mathbf{u}^{\varepsilon_0, i} - \nabla_x \cdot \boldsymbol{\sigma}^{\varepsilon_0, i} - \nabla_y \cdot \boldsymbol{\sigma}^{\varepsilon_0, i+1} = \mathbf{f} \delta_{i,0}, \quad (25)$$

$$\boldsymbol{\sigma}^{\varepsilon_0, i} = \mathbf{c}^{\varepsilon_0} : (\boldsymbol{\epsilon}_x(\mathbf{u}^{\varepsilon_0, i}) + \boldsymbol{\epsilon}_y(\mathbf{u}^{\varepsilon_0, i+1})). \quad (26)$$

To solve this homogenization problem up to the order i_0 , (25) and (26) need to be solved for each i , up to i_0 . This is the purpose of the next section.

3.4 Resolution of the homogenization problem

3.4.1 Order 0 solution and first order corrector

The resolution of the system (25,26) is classical and can be found for example in Sanchez-Palencia (1980) or in Guillot *et al.* (2010). We therefore just recall the main results and one could refer to Guillot *et al.* (2010) for a complete development. Solving (25) and (26), it is first found that $\sigma^{-1} = 0$ and that $\mathbf{u}^{\varepsilon_0,0} = \langle \mathbf{u}^{\varepsilon_0,0} \rangle$. The last equality implies that $\mathbf{u}^{\varepsilon_0,0}$ doesn't depend upon the fast variable \mathbf{y} . This is an important result that is intuitively well known: to the order 0 the displacement field doesn't contain any fast variation (that is, is insensitive to small scale heterogeneities). Nevertheless, $\sigma^{\varepsilon_0,0} \neq \langle \sigma^{\varepsilon_0,0} \rangle$ to the contrary of the 1D case (Capdeville *et al.*, 2010). It can be shown that $\mathbf{u}^{\varepsilon_0,0}$ is solution of the following effective equations:

$$\begin{aligned} \rho^{*\varepsilon_0} \partial_{tt} \mathbf{u}^{\varepsilon_0,0} - \nabla \cdot \langle \sigma^{\varepsilon_0,0} \rangle &= \mathbf{f}, \\ \langle \sigma^{\varepsilon_0,0} \rangle &= \mathbf{c}^{*\varepsilon_0} : \epsilon_x(\mathbf{u}^{\varepsilon_0,0}), \end{aligned} \quad (27)$$

where $\mathbf{c}^{*\varepsilon_0}$ and $\rho^{*\varepsilon_0}$ are the order 0 effective elastic tensor and density. Let χ^{ε_0} be the so-called first-order corrector, a 3rd order tensor build of the collections of first order correctors (which are vectors), solution in \mathcal{V} of

$$\partial_{y_i} H_{ijkl}^{\varepsilon_0} = 0, \quad (28)$$

with

$$H_{ijkl}^{\varepsilon_0} = c_{ijmn}^{\varepsilon_0} G_{mnkl}^{\varepsilon_0}, \quad (29)$$

$$G_{ijkl}^{\varepsilon_0} = \frac{1}{2} \left(\delta_{ik} \delta_{jl} + \delta_{jk} \delta_{il} + \partial_{y_i} \chi_j^{\varepsilon_0,kl} + \partial_{y_j} \chi_i^{\varepsilon_0,kl} \right). \quad (30)$$

It can be shown that the effective elastic tensor simply is

$$\mathbf{c}^{*\varepsilon_0}(\mathbf{x}) = \langle \mathbf{H}^{\varepsilon_0} \rangle(\mathbf{x}). \quad (31)$$

For the density, it can be shown that we simply have $\rho^{*\varepsilon_0} = \langle \rho^{\varepsilon_0} \rangle$.

At this stage, solving the effective equations (27), $\mathbf{u}^{\varepsilon_0,0}$ and the average stress $\langle \sigma^{\varepsilon_0,0} \rangle$ can be found. To obtain the complete order 0 stress tensor, $\sigma^{\varepsilon_0,0}$ needs to be computed using

$$\sigma^{\varepsilon_0,0}(\mathbf{x}, \mathbf{y}) = \mathbf{H}^{\varepsilon_0}(\mathbf{x}, \mathbf{y}) : \epsilon_x(\mathbf{u}^{\varepsilon_0,0}(\mathbf{x})). \quad (32)$$

The order 1 solution can be written as

$$u_i^{\varepsilon_0,1}(\mathbf{x}, \mathbf{y}) = \chi_i^{\varepsilon_0,kl}(\mathbf{x}, \mathbf{y}) \epsilon_{x,kl}^{\varepsilon_0,0}(\mathbf{x}) + \langle u_i^{\varepsilon_0,1} \rangle(\mathbf{x}). \quad (33)$$

where $\epsilon_x^{\varepsilon_0,0} = \epsilon_x(\mathbf{u}^{\varepsilon_0,0})$. In this paper, we stop our development to the order 0 and first order correction, which means we do not solve for $\langle \mathbf{u}^{\varepsilon_0,1} \rangle$. For the 1D case, $\langle \mathbf{u}^{\varepsilon_0,1} \rangle$ is always equal to zero (see Capdeville *et al.* 2010), but for higher dimension problems like the one we tackle here, $\langle \mathbf{u}^{\varepsilon_0,1} \rangle$ is not equal to zero in general. Nevertheless we will notice in the examples that it might be very small, in some cases at least.

Finally, note that the physical interpretation of the effective elastic tensor formula (31) is not obvious. It can be interpreted as the average of the elastic tensor, plus a correction made of the average of the elementary stresses associated to the displacements $\chi^{\varepsilon_0,kl}$. This interpretation can be linked to an heuristic approach to obtain an effective elastic tensor by computing the average stresses and strains associated to a set of elementary static problems and finding the average tensor linking them. This approach is known as the “average method”, and was developed by Suquet (1982). This idea has been used in the dynamical case by Grechka (2003), but for a set of elementary problems based on a set of boundary conditions applied to the unit cell instead of a set of external forces.

3.4.2 Practical resolution

Practically, to solve the homogenized equations, presented in the previous section, with classical wave equation solver like SEM, different orders are combined together (Fish & Chen, 2004; Capdeville & Marigo, 2007; Capdeville & Marigo, 2008; Capdeville *et al.*, 2010):

$$\langle \hat{\mathbf{u}}^{\varepsilon_0,\varepsilon,i} \rangle(\mathbf{x}) = \mathbf{u}^{\varepsilon_0,0}(\mathbf{x}) + \varepsilon \langle \mathbf{u}^{\varepsilon_0,1} \rangle(\mathbf{x}) + \dots + \varepsilon^i \langle \mathbf{u}^{\varepsilon_0,i} \rangle(\mathbf{x}), \quad (34)$$

$$\langle \hat{\boldsymbol{\sigma}}^{\varepsilon_0,\varepsilon,i} \rangle(\mathbf{x}) = \langle \boldsymbol{\sigma}^{\varepsilon_0,0} \rangle(\mathbf{x}) + \varepsilon \langle \boldsymbol{\sigma}^{\varepsilon_0,1} \rangle(\mathbf{x}) + \dots + \varepsilon^i \langle \boldsymbol{\sigma}^{\varepsilon_0,i} \rangle(\mathbf{x}), \quad (35)$$

where $\langle \hat{\boldsymbol{\sigma}}^{\varepsilon_0,\varepsilon,i} \rangle$ and $\langle \hat{\mathbf{u}}^{\varepsilon_0,\varepsilon,i} \rangle$ are solutions of an order i combined effective equation. Knowing $\langle \hat{\mathbf{u}}^{\varepsilon_0,\varepsilon,i} \rangle$, $\hat{\mathbf{u}}^{\varepsilon_0,\varepsilon,i}$ can be found using an high corrector operator that we won't explicit here and it can be shown that

$$\mathbf{u}^{\varepsilon_0,\varepsilon}(\mathbf{x}) = \hat{\mathbf{u}}^{\varepsilon_0,\varepsilon,i}(\mathbf{x}) + O(\varepsilon^{i+1}). \quad (36)$$

In the present article, because we stop the expansion at the order 0, $\langle \hat{\mathbf{u}}^{\varepsilon_0,\varepsilon,0} \rangle$ and $\langle \hat{\boldsymbol{\sigma}}^{\varepsilon_0,\varepsilon,0} \rangle$ are simply $\mathbf{u}^{\varepsilon_0,0}$ and $\langle \boldsymbol{\sigma}^{\varepsilon_0,0} \rangle$ and the combined effective equation is simply the equation (27). At the order 0, the solutions $\hat{\mathbf{u}}^{\varepsilon_0,\varepsilon,0}$ and $\hat{\boldsymbol{\sigma}}^{\varepsilon_0,\varepsilon,0}$ are

$$\hat{\mathbf{u}}^{\varepsilon_0,\varepsilon,0}(\mathbf{x}) = \langle \hat{\mathbf{u}}^{\varepsilon_0,\varepsilon,0} \rangle, \quad (37)$$

$$\hat{\boldsymbol{\sigma}}^{\varepsilon_0,\varepsilon,0}(\mathbf{x}) = \mathbf{H}^{\varepsilon_0}(\mathbf{x}, \mathbf{x}/\varepsilon) : \epsilon_x(\hat{\mathbf{u}}^{\varepsilon_0,\varepsilon,0}(\mathbf{x})) \quad (38)$$

Applying the first order corrector to $\hat{\mathbf{u}}^{\varepsilon_0, \varepsilon, 0}(\mathbf{x})$, we can obtain a partial order 1 solution

$$\hat{\mathbf{u}}^{\varepsilon_0, \varepsilon, 1/2}(\mathbf{x}) = \langle \hat{\mathbf{u}}^{\varepsilon_0, \varepsilon, 0} \rangle(\mathbf{x}) + \chi^{\varepsilon_0}(\mathbf{x}, \mathbf{x}/\varepsilon) : \epsilon_x \left(\langle \hat{\mathbf{u}}^{\varepsilon_0, \varepsilon, 0} \rangle \right)(\mathbf{x}), \quad (39)$$

where the $1/2$ superscript means “partial order 1”. To obtain a complete order 1 solution, $\langle \mathbf{u}^{\varepsilon_0, 1} \rangle$ should be computed, which we won’t do here. Because, it is only a partial order 1 solution, we do not have in general

$$\mathbf{u}^{\varepsilon_0, \varepsilon}(\mathbf{x}) = \hat{\mathbf{u}}^{\varepsilon_0, \varepsilon, 1/2}(\mathbf{x}) + O(\varepsilon^2), \quad (40)$$

on the contrary of the 1D case (in the 1D case, $\langle \mathbf{u}^{\varepsilon_0, 1} \rangle$ can be shown to be 0, see Capdeville *et al.* (2010)), unless $\langle \mathbf{u}^{\varepsilon_0, 1} \rangle$ is very small, which appears to be the case at least for the random square example presented in this paper.

Finally, the only ε that is of practical interest is $\varepsilon = \varepsilon_0$ as, thanks to (20), it is the only case for which $\mathbf{u}^{\varepsilon_0, \varepsilon}$ is equal to the solution of the original problem \mathbf{u}^{ref} . Note that, for all ε_0 , we have $\mathbf{u}^{ref} = \mathbf{u}^{\varepsilon_0, \varepsilon_0}$. Using the above development, we therefore have $\mathbf{u}^{ref}(\mathbf{x}) = \hat{\mathbf{u}}^{\varepsilon_0, \varepsilon_0, 0}(\mathbf{x}) + O(\varepsilon_0)$.

3.4.3 External source term

We have shown in a previous work (Capdeville *et al.*, 2010) that, for an external point source, the original force or the moment tensor should be corrected. As in this article we stop the asymptotic expansion at the order 0, nothing needs to be done for a vector force, which is not the case for a moment tensor. For a moment tensor located in \mathbf{x}_0 , the external force is

$$\mathbf{f}(\mathbf{x}, t) = g(t) \mathbf{M} \cdot \nabla \delta(\mathbf{x} - \mathbf{x}_0) \quad (41)$$

where $g(t)$ is the source time wavelet and \mathbf{M} the symmetric moment tensor. As shown by Capdeville *et al.* (2010), we need to find a moment tensor $\mathbf{M}^{\varepsilon_0, \varepsilon, 0}$ such that

$$(\mathbf{u}^{\varepsilon_0, \varepsilon}, \mathbf{f}) = (\langle \mathbf{u}^{\varepsilon_0, \varepsilon, 0} \rangle, \mathbf{f}^{\varepsilon_0, \varepsilon, 0}) + O(\varepsilon), \quad (42)$$

where (\cdot, \cdot) is the L^2 inner product and

$$\mathbf{f}^{\varepsilon_0, \varepsilon, 0}(\mathbf{x}, t) = g(t) \mathbf{M}^{\varepsilon_0, \varepsilon, 0} \cdot \nabla \delta(\mathbf{x} - \mathbf{x}_0). \quad (43)$$

Using an integration by parts and the symmetry of the moment tensor, (42) becomes

$$\mathbf{M} : \epsilon(\mathbf{u}^{\varepsilon_0, \varepsilon})|_{\mathbf{x}_0} = \mathbf{M}^{\varepsilon_0, \varepsilon, 0} : \epsilon_x(\langle \mathbf{u}^{\varepsilon_0, \varepsilon, 0} \rangle)|_{\mathbf{x}_0} + O(\varepsilon). \quad (44)$$

Using (23) and (33), one finally finds, at the order 0

$$\mathbf{M}^{\varepsilon_0, \varepsilon, 0} = \mathbf{G}^{\varepsilon_0}(\mathbf{x}_0, \mathbf{x}_0/\varepsilon) : \mathbf{M}. \quad (45)$$

3.5 Construction of $\rho^{\varepsilon_0}(\mathbf{x}, \mathbf{y})$ and $\mathbf{c}^{\varepsilon_0}(\mathbf{x}, \mathbf{y})$

The next (and essential) step, is to build ρ^{ε_0} and $\mathbf{c}^{\varepsilon_0}(\mathbf{x}, \mathbf{y})$ such that $\mathbf{u}^{\varepsilon_0,0}$, $\mathbf{u}^{\varepsilon_0,1}$ and $\boldsymbol{\sigma}^{\varepsilon_0,0}$ are in \mathcal{V} .

It can be seen from (33) and (32) that $\mathbf{u}^{\varepsilon_0,0}$, $\mathbf{u}^{\varepsilon_0,1}$ and $\boldsymbol{\sigma}^{\varepsilon_0,0}$ are in \mathcal{V} if $\mathbf{c}^{\varepsilon_0}(\mathbf{x}, \mathbf{y})$ can be build such that χ^{ε_0} and $\mathbf{H}^{\varepsilon_0}$ are in \mathcal{V} . Note that if this is the case, $\mathbf{G}^{\varepsilon_0}$ is also in \mathcal{V} (gradients of function in \mathcal{V} are also in \mathcal{V}). Therefore, we seek for $\rho^{\varepsilon_0}(\mathbf{x}, \mathbf{y})$ and $\mathbf{c}^{\varepsilon_0}(\mathbf{x}, \mathbf{y})$ such that

- (i) ρ^{ε_0} , $\mathbf{H}^{\varepsilon_0}$ and $\chi^{\varepsilon_0,kl}$ are in \mathcal{V} ;
- (ii) ρ^{ε_0} and $\mathbf{c}^{\varepsilon_0}$ must be positive definite;
- (iii) $\rho^{\varepsilon_0}(\mathbf{x}, \mathbf{x}/\varepsilon_0) = \rho^0(\mathbf{x})$ and $\mathbf{c}^{\varepsilon_0}(\mathbf{x}, \mathbf{x}/\varepsilon_0) = \mathbf{c}^0(\mathbf{x})$.

The construction of $\rho^{\varepsilon_0}(\mathbf{x}, \mathbf{y})$ is trivial. To do so, we introduce a initial $\rho^{\varepsilon_0,s}(\mathbf{x}, \mathbf{y}) = \rho^0(\varepsilon_0 \mathbf{y})$ defined on $\mathbb{R} \times \mathbf{Y}_{\mathbf{x}}$ and then extended to \mathbb{R}^2 in \mathbf{y} by periodicity. $\rho^{\varepsilon_0,s}$ depends on \mathbf{x} because the cell domain used in \mathbf{y} , $\mathbf{Y}_{\mathbf{x}}$, depends on \mathbf{x} . If the \mathbf{Y}_0 cell is chosen as a the whole domain, then this \mathbf{x} dependence disappears. We can then define

$$\rho^{\varepsilon_0}(\mathbf{x}, \mathbf{y}) = \mathcal{F}(\rho^{\varepsilon_0,s})(\mathbf{x}, \mathbf{x}/\varepsilon_0) + (\rho^{\varepsilon_0,s} - \mathcal{F}(\rho^{\varepsilon_0,s}))(\mathbf{x}, \mathbf{y}). \quad (46)$$

We indeed have $\rho^{\varepsilon_0,s}$ is in \mathcal{T} , $\rho^{\varepsilon_0}(\mathbf{x}, \mathbf{x}/\varepsilon_0) = \rho^0(\mathbf{x})$ and ρ^{ε_0} is in \mathcal{V} and is a positive function with a well chosen wavelet w_m . Moreover, with such a definition, we have,

$$\rho^{*\varepsilon_0} = \langle \rho^{\varepsilon_0} \rangle = \mathcal{F}(\rho^{\varepsilon_0,s}) \quad (47)$$

For $\mathbf{c}^{\varepsilon_0}$, the process is not trivial and we follow the procedure describe by Capdeville *et al.* (2010) and Guillot *et al.* (2010) which is inspired by the homogenization procedure for random media (Papanicolaou & Varadhan, 1979). The main idea is to search for two intermediate fields $\mathbf{G}^{\varepsilon_0}$ and $\mathbf{H}^{\varepsilon_0}$ in \mathcal{V} such that $\mathbf{G}^{\varepsilon_0}$ can be written as

$$\mathbf{G}^{\varepsilon_0} = \frac{1}{2} (\nabla_y \chi^{\varepsilon_0} + {}^t \nabla_y \chi^{\varepsilon_0}) + \mathbf{I}^4, \quad (48)$$

and

$$\mathbf{H}^{\varepsilon_0} = \mathbf{c}^{\varepsilon_0} : \mathbf{G}^{\varepsilon_0}, \quad (49)$$

$$\nabla_y \cdot \mathbf{H}^{\varepsilon_0} = 0, \quad (50)$$

$$\langle \mathbf{G}^{\varepsilon_0} \rangle = \mathbf{I}^4, \quad (51)$$

where $[\nabla_y \chi^{\varepsilon_0}]_{ijkl} = \partial_{y_i} \chi_j^{\varepsilon_0,kl}$, $[{}^t \nabla_y \chi^{\varepsilon_0}]_{ijkl} = \partial_{y_j} \chi_i^{\varepsilon_0,kl}$ and $I_{ijkl}^4 = \frac{1}{2} (\delta_{ik} \delta_{jl} + \delta_{jk} \delta_{il})$.

To do so, we propose the following procedure:

- Step 1: build a start $\mathbf{c}^{\varepsilon_0,s}$ defined as $\mathbf{c}^{\varepsilon_0,s}(\mathbf{x}, \mathbf{y}) = \mathbf{c}^0(\varepsilon_0 \mathbf{y})$ for \mathbf{y} in $\mathbf{Y}_{\mathbf{x}}$ and then extended to \mathbb{R}^2 by periodicity. Then solve (28) with periodic boundary conditions in $\mathbf{Y}_{\mathbf{x}}$ to find $\chi_s^{\varepsilon_0,kl}(\mathbf{x}, \mathbf{y})$.

- Step 2: compute

$$\mathbf{G}^{\varepsilon_0,s}(\mathbf{x}, \mathbf{y}) = \frac{1}{2} (\nabla_y \chi^{\varepsilon_0,s} + {}^t \nabla_y \chi^{\varepsilon_0,s}) + \mathbf{I}^4, \quad (52)$$

$$\mathbf{H}^{\varepsilon_0,s}(\mathbf{x}, \mathbf{y}) = \mathbf{c}^{\varepsilon_0,s}(\mathbf{x}, \mathbf{y}) : \mathbf{G}^{\varepsilon_0,s}(\mathbf{x}, \mathbf{y}). \quad (53)$$

$\mathcal{F}(\mathbf{G}^{\varepsilon_0,s})$ being symmetric and, for well chosen wavelet w_m , positive definite, it can be inverted.

This allows to build, for any $\mathbf{y} \in \mathbf{Y}_x$,

$$\mathbf{G}^{\varepsilon_0}(\mathbf{x}, \mathbf{y}) = [(\mathbf{G}^{\varepsilon_0,s} - \mathcal{F}(\mathbf{G}^{\varepsilon_0,s}))(\mathbf{x}, \mathbf{y})] : [\mathcal{F}(\mathbf{G}^{\varepsilon_0,s})(\mathbf{x}, \mathbf{x}/\varepsilon_0)]^{-1} + \mathbf{I}^4, \quad (54)$$

$$\mathbf{H}^{\varepsilon_0}(\mathbf{x}, \mathbf{y}) = [(\mathbf{H}^{\varepsilon_0,s} - \mathcal{F}(\mathbf{H}^{\varepsilon_0,s}))(\mathbf{x}, \mathbf{y}) + \mathcal{F}(\mathbf{H}^{\varepsilon_0,s})(\mathbf{x}, \mathbf{x}/\varepsilon_0)] : [\mathcal{F}(\mathbf{G}^{\varepsilon_0,s})(\mathbf{x}, \mathbf{x}/\varepsilon_0)]^{-1}. \quad (55)$$

The $\mathbf{G}^{\varepsilon_0}$ and $\mathbf{H}^{\varepsilon_0}$ extension from \mathbf{Y}_x to \mathbb{R}^2 in \mathbf{y} is then done by periodicity.

- Step 3: From (49) we can build

$$\mathbf{c}^{\varepsilon_0}(\mathbf{x}, \mathbf{y}) = \left(\mathbf{H}^{\varepsilon_0} : (\mathbf{G}^{\varepsilon_0})^{-1} \right) (\mathbf{x}, \mathbf{y}). \quad (56)$$

Using (54) and (55) in (56), it can be seen that the tensor to be inverted in the above equation, is in fact $(\mathbf{G}^{\varepsilon_0,s} - \mathcal{F}(\mathbf{G}^{\varepsilon_0,s}))(\mathbf{x}, \mathbf{y}) + \mathcal{F}(\mathbf{G}^{\varepsilon_0,s})(\mathbf{x}, \mathbf{x}/\varepsilon_0)$. The latter is symmetric and positive definite for well chosen wavelet w_m , meaning it can be inverted and that (56) can be computed. It can be also note that

$$\mathbf{c}^{*,\varepsilon_0}(\mathbf{x}) = \langle \mathbf{H}^{\varepsilon_0} \rangle (\mathbf{x}) = \left(\mathcal{F}(\mathbf{H}^{\varepsilon_0,s}) : \mathcal{F}(\mathbf{G}^{\varepsilon_0,s})^{-1} \right) (\mathbf{x}, \mathbf{x}/\varepsilon_0). \quad (57)$$

- Step 4: once $\mathbf{c}^{\varepsilon_0}(\mathbf{x}, \mathbf{y})$ is known, the whole classical homogenization procedure can be pursued.

Remark: in practical cases, the domain is finite and \mathbf{Y}_x can be chosen to enclose the whole domain. In that case, the dependence to the macroscopic location \mathbf{x} in $\chi^{\varepsilon_0,kl}$, $\mathbf{G}^{\varepsilon_0,s}$, $\mathbf{H}^{\varepsilon_0,s}$ and $\mathbf{c}^{\varepsilon_0,s}$ disappears.

Following these steps, we indeed have by construction $\mathbf{c}^{\varepsilon_0}(\mathbf{x}, \mathbf{x}/\varepsilon_0) = \mathbf{c}^0(\mathbf{x})$ and $\mathbf{c}^{\varepsilon_0}$ is positive definite for a well chosen wavelet w_m . It is also important to check that, at the end of the procedure, $\chi^{\varepsilon_0,kl}$ is indeed in \mathcal{V} ($\mathbf{H}^{\varepsilon_0}$ is in \mathcal{V} by construction). At step 2, we have, by construction, $(\mathbf{H}^{\varepsilon_0}, \mathbf{G}^{\varepsilon_0}) \in \mathcal{V}$ and $\langle \mathbf{G}^{\varepsilon_0} \rangle = \mathbf{I}^4$. $\mathbf{G}^{\varepsilon_0}$ can be written under the form (48) if, and only if, $\nabla_y \times \mathbf{G}^{\varepsilon_0} = 0$. Knowing that for any \mathbf{h} , $\nabla_y \times \mathcal{F}(\mathbf{h}) = \mathcal{F}(\nabla_y \times \mathbf{h})$, and that, $\nabla_y \times \mathbf{G}^{\varepsilon_0,s} = 0$, we indeed have $\nabla_y \times \mathbf{G}^{\varepsilon_0} = 0$. It therefore exists a corrector $\chi^{\varepsilon_0,kl}$ such that (48) can be written. Furthermore, knowing that for any \mathbf{h} and \mathbf{g} such $\mathbf{h} = \nabla_y \mathbf{g}$, $\mathbf{h} \in \mathcal{V}$ with $\langle \mathbf{h} \rangle = 0$ implies that \mathbf{g} lies in \mathcal{V} , we indeed have $\chi^{\varepsilon_0,kl}$ in \mathcal{V} . At this stage we have found $\mathbf{H}^{\varepsilon_0}$ and $\mathbf{G}^{\varepsilon_0}$, unique solutions to our problem, and we know it exists a $\chi^{\varepsilon_0,kl}$ in \mathcal{V} satisfying (48). We ensure the uniqueness of $\chi^{\varepsilon_0,kl}$ by imposing $\langle \chi^{\varepsilon_0,kl} \rangle = 0$. To find $\chi^{\varepsilon_0,kl}$, we can either solve (48), or find $\mathbf{c}^{\varepsilon_0}$ with (56) and solve again (28). We have chosen this last alternative. An illustration of the process is sketched in Fig. 10. It can be seen that the power spectrum component

of the corrector which is represented (lower right graph) is equal to zero for $|\mathbf{k}|/\varepsilon_0 < 6.10^{-3}m^{-1}$ which implies it belongs to \mathcal{V} .

One can notice that the symmetry of the effective elastic tensor does not appear to be obvious from (57). Though we can show that, in the periodic case and for layered media, (57) analytically gives a symmetric elastic tensor (Guillot *et al.*, 2010). We are not able to prove it in the general case for the time being. Let us define the skewness of the effective elastic tensor as

$$d(\mathbf{x}) = \frac{\max(\mathbf{c}^* - {}^t\mathbf{c}^*)}{\max(\mathbf{c}^*)}(\mathbf{x}), \quad (58)$$

where the \max operator applies to the tensor components. In practice, a slight skewness of the effective elastic tensor can be observed for the examples studied in this paper: typically d takes values below 10^{-3} with some localized peaks attaining 10^{-2} . Using the same algorithm on periodic or layered media, we get values of the order of 10^{-5} . At this point, we do not know if the effective tensor indeed has a slight skewness for general media or if this is just an accuracy issue. This important point deserves to be studied in a future work.

4 VALIDATION TESTS

In order to validate our development, we apply the homogenization procedure to the two model examples studied in subsections 2.4.1 and 2.4.2. To do so we need to solve the cell problem (28) on the whole domain with periodic boundary conditions (we choose \mathbf{Y}_x as the whole domain). Note that one could rather choose to solve the cell problem on multiple smaller domains. This solution is not necessary in 2D but might be interesting in 3D or for very large domains in 2D. We use a relatively high order finite element method based on a triangular mesh to solve the weak (or variational) form of the cell problem equations. The finite element interpolation is based on the Fekete points (Pasquetti & Rapetti, 2004; Mercierat *et al.*, 2006) and we employ an high order integration quadrature (Rathod *et al.*, 2004). In the following two examples, the polynomial expansion used over each element corresponds to a degree 5 polynomial order on elements' edge.

4.1 First example: square random model

We first apply the non-periodic homogenization procedure to the random square model described in section 2.4.1. The spatial low-pass filter is the same, and so is the value of the ε_0 parameter (which is then equal to 0.3). In figure Fig. 11 are shown V_s (left plot) and the total anisotropy (right plot) computed from the order 0 homogenized coefficients ρ^{*,ε_0} and $\mathbf{c}^{*,\varepsilon_0}$. At any given location \mathbf{x} , the maximum anisotropy is defined by: $\max\{|\mathbf{c}^{*,\varepsilon_0} - \mathbf{c}_{iso}^{*,\varepsilon_0}|\}/\max\{\mathbf{c}_{iso}^{*,\varepsilon_0}\}$, where $\mathbf{c}_{iso}^{*,\varepsilon_0}$ is the closest isotropic elastic

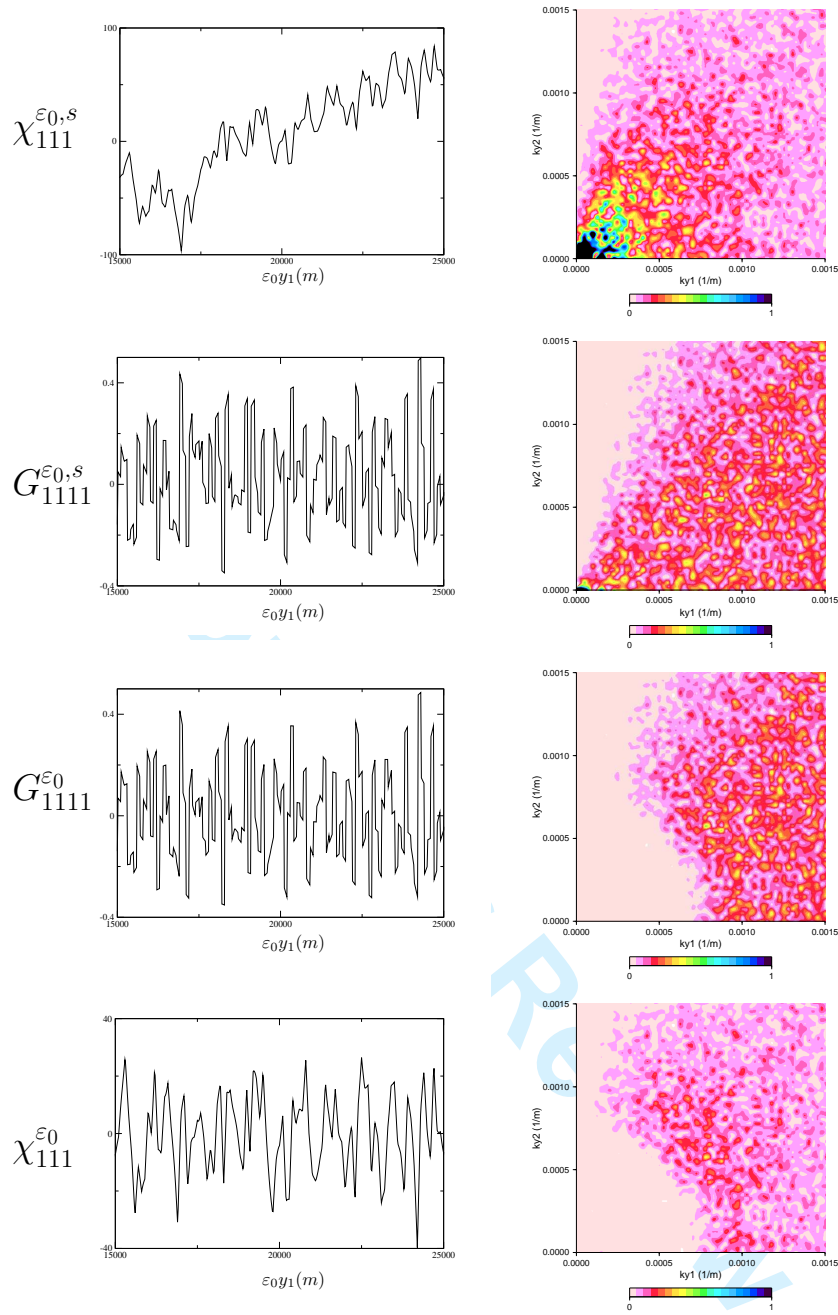


Figure 10. Illustration of the construction of the correctors in \mathcal{V} . On the left column are plotted $\chi_{s,1}^{\varepsilon_0,11}(y_1, y_2)$, $G_{1111}^{\varepsilon_0,s}(y_1, y_2)$, $G_{1111}^{\varepsilon_0}(\mathbf{x}_0, y_1, y_2)$ and $\chi_1^{\varepsilon_0,11}(\mathbf{x}_0, y_1, y_2)$ as a function of $\varepsilon_0 y_1$ for $\varepsilon_0 y_2 = 20 \text{ km}$ and $\mathbf{x}_0 = {}^t(20 \text{ km}, 20 \text{ km})$. On the right column are plotted $|\bar{\chi}_{s,1}^{\varepsilon_0,11}|(\mathbf{k}_y)$, $|\bar{G}_{1111}^{\varepsilon_0,s}|(\mathbf{k}_y)$, $|\bar{G}_{1111}^{\varepsilon_0}|(\mathbf{x}_0, \mathbf{k}_y)$ and $|\bar{\chi}_1^{\varepsilon_0,11}|(\mathbf{x}_0, \mathbf{k}_y)$ at $\mathbf{x}_0 = {}^t(20 \text{ km}, 20 \text{ km})$ and for positive wavenumbers. The actual ε_0 corresponds to the wavelet shown in Fig. 1.

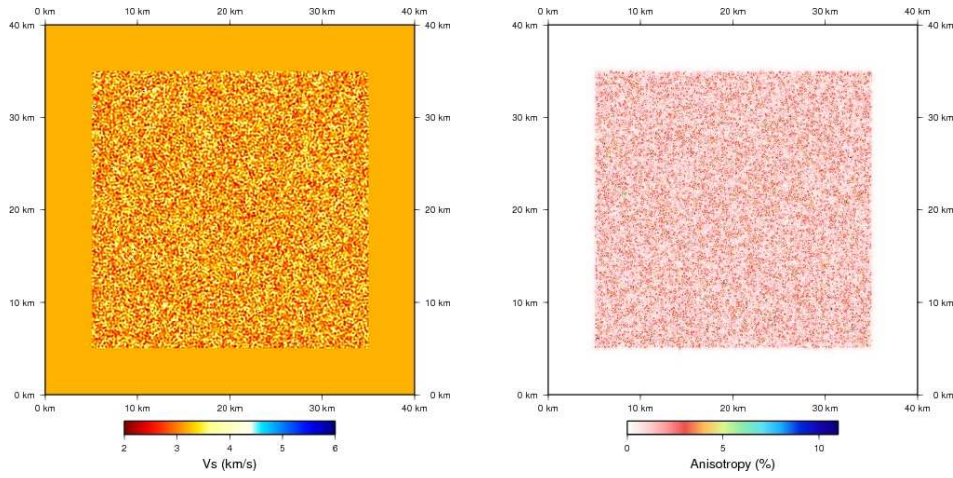


Figure 11. Leading order homogenized model of the “square” model (see Fig. 2). $V_s = \sqrt{c_{2222}^{\varepsilon_0,*}/\rho^{\varepsilon_0,*}}$ and the total anisotropy are presented. The total anisotropy is computed, at a given location \mathbf{x} , as $\max\{|\mathbf{c}^{*,\varepsilon_0} - \mathbf{c}_{iso}^{*,\varepsilon_0}|\}/\max\{\mathbf{c}_{iso}^{*,\varepsilon_0}\}$, where $\mathbf{c}_{iso}^{*,\varepsilon_0}$ is the closest isotropic elastic tensor to $\mathbf{c}^{*,\varepsilon_0}$.

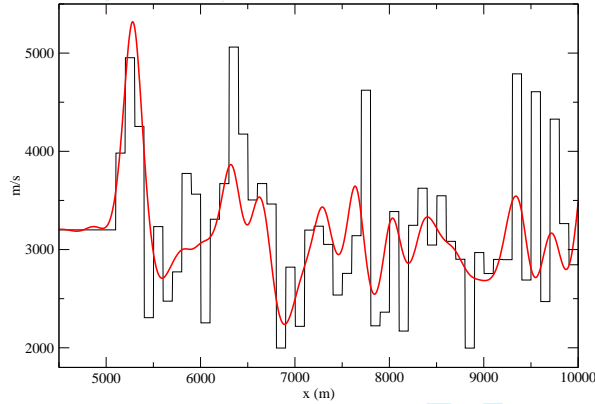


Figure 12. Black line: 1D section of V_s at $x_2 = 32 \text{ km}$ as a function of x_1 or the original “square” model (see Fig. 2). Red line: 1D section of $V_s = \sqrt{c_{2222}^{\varepsilon_0,*}/\rho^{\varepsilon_0,*}}$ at $x_2 = 32 \text{ km}$ as a function of x_1 for the homogenized model (see Fig. 11.)

to $\mathbf{c}^{*,\varepsilon_0}$ (in the sens of, for example, Browaeys & Chevrot 2004). The homogenized quantities also show rapid spatial variations, but these are smoother than for the original medium as can be seen for V_s along a section in Fig. 12. The apparent anisotropy is significant with average values around 2.5% and peak values up to 11%. In Fig. 13 is shown a comparison of the order 0 homogenized solution with the filtered wave velocities solution (alternative (i) of section 2.4.1) for source A and receiver 22. In the left column plots, we compare the x_1 component of the order 0 homogenized velocity ($\dot{u}_1^{\varepsilon_0,0}$, in red line) to the reference solution (black line) as a function of ε_0 (from 2.4 to 0.3). On the right column is presented the same but for the filtered wave velocities solution. It appears clearly, that when both upscaling processes are used with a large ε_0 , that is too much smoothing with respect to λ_{min} ,

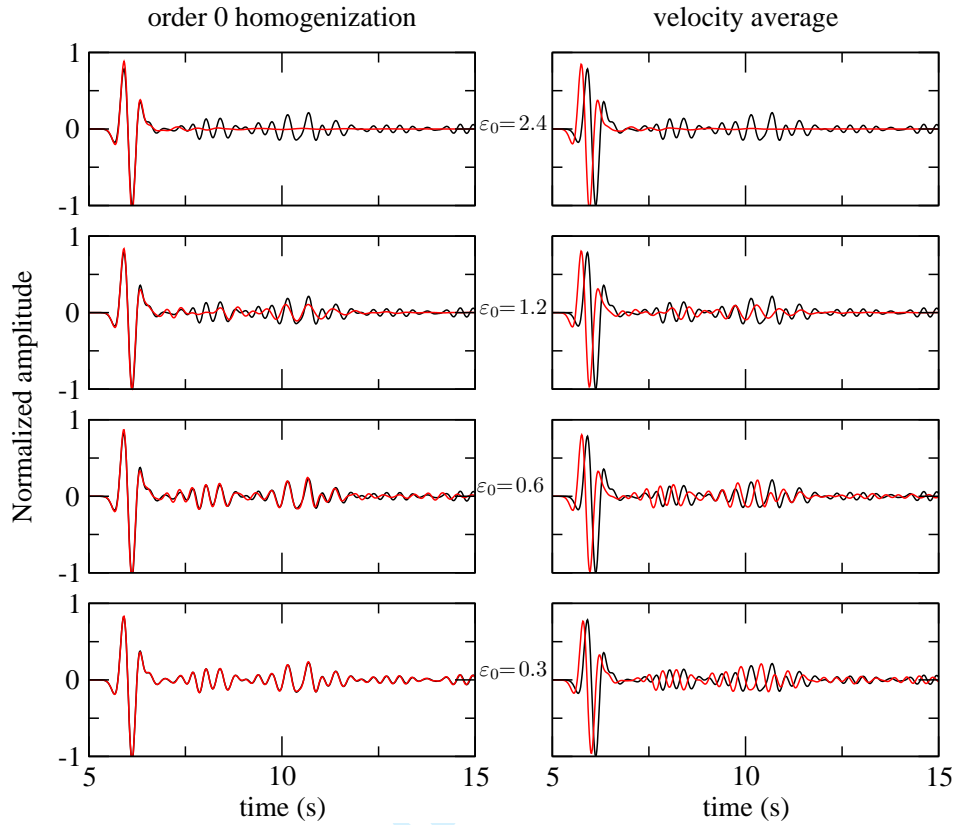


Figure 13. x_1 component velocity traces computed for the source A at receiver 22 for the reference solution (black line), for the order 0 homogenized solution ($\dot{u}_1^{\varepsilon_0,0}$, left column, red line) and for the velocity filtering upscaled model (right column, red line) for $\varepsilon_0 = 2.4, 1.2, 0.6$ and 0.3 .

the coda of the direct wave disappears. Nevertheless, the ballistic P wave has a correct time arrival for the homogenized solution, whereas this not the case for the filtered wave velocities solution. When ε_0 decreases, that is when more and more details are incorporated in the upscaled model, the coda wave appears. Nevertheless, once again, the phase correctly predicted only for the homogenized solution and it seems that the filtered velocities solution have a very poor convergence with ε_0 . To look more closely at the convergence issue, we define the error $E_i(\dot{\mathbf{u}})$ of a solution in velocity $\dot{\mathbf{u}}$ at a given receiver i

$$E_i(\dot{\mathbf{u}}) = \frac{\sqrt{\int_0^{t_{max}} (\dot{\mathbf{u}} - \dot{\mathbf{u}}^{ref})^2(\mathbf{x}_i, t) dt}}{\sqrt{\int_0^{t_{max}} (\dot{\mathbf{u}}^{ref})^2(\mathbf{x}_i, t) dt}}, \quad (59)$$

where \mathbf{u}^{ref} is the reference solution and t_{max} is here 20 s. We defined the combined error from receiver 5 to receiver 35 (see Fig. 3) as

$$E_c(\dot{\mathbf{u}}) = \frac{1}{31} \sum_{i=5}^{35} E_i(\dot{\mathbf{u}}). \quad (60)$$

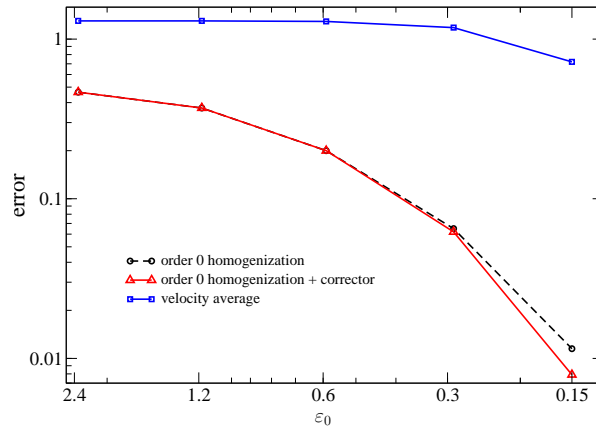


Figure 14. Combined error as defined by equation (60) as a function of ε_0 for an explosion located in A (see Fig. 3) for the solution computed in the velocity filtering upscaled model (blue line), for the order 0 homogenized solution ($\dot{\mathbf{u}}^{\varepsilon_0,0}$, in red line) and for the order 0 homogenized plus first order correction ($\dot{\mathbf{u}}^{\varepsilon_0,1/2}$ as defined by (39), in dashed black line).

In Fig. 14 is shown the error as defined above for a wave propagation computed for source A (see Fig. 3) as a function of ε_0 . It clearly appears that the error for the filtered wave velocity model solution has a very poor convergence with ε_0 . Furthermore, as it could already be seen in Fig. 13, this error is much larger than the one obtained for the homogenized solution. For the order 0 homogenized solution, the error $E^c(\dot{\mathbf{u}}^{\varepsilon_0,0})$ decreases first slowly for large ε_0 . This can be understood in Fig. 13, left column: the coda is fully constructed only for $\varepsilon_0 \leq 0.6$. Once the coda is fully constructed, the convergence is unexpectedly fast (in between ε_0^2 and ε_0^3) whereas we should expect a convergence in ε_0 only. This fact certainly implies that, at least for this specific example, higher order terms of the asymptotic expansion are very small with respect to the leading term. This is confirmed by the introduction of the first order correction in the calculation of the error $E_c(\dot{\mathbf{u}}^{\varepsilon_0,1/2})$: its effect can be observed only for the smallest ε_0 values. For very small ε_0 , we expect that the error convergence of the leading term would decrease as ε_0 , rather than as ε_0^2 . The effect of the first order correction can nevertheless clearly be seen by improving the fit for small values of ε_0 . This can also be seen in Fig. 15 where the error for the order 0 homogenized solution, $E_i(\dot{\mathbf{u}}^{\varepsilon_0,0})$, and for the order 0 homogenized solution supplemented by the first order correction, $E_i(\dot{\mathbf{u}}^{\varepsilon_0,1/2})$, for receivers 5 to 35 are plotted as a function of their location along the x_1 axis and for $\varepsilon_0 = 0.15$. It clearly appears that, when adding the first order correction to the leading term of the expansion, the error is, as expected, always minimized. An interesting observation is that the error determined for the sole leading term varies more rapidly with x_1 than when the first order correction is taken into account. This is expected since the fast scale (y) dependence of the first order correction implies variations of the wavefield at the microscopic scale. Note that this error as a function of x_1 is largely under-sampled in Fig. 15 as we only have one receiver every 1km compared to

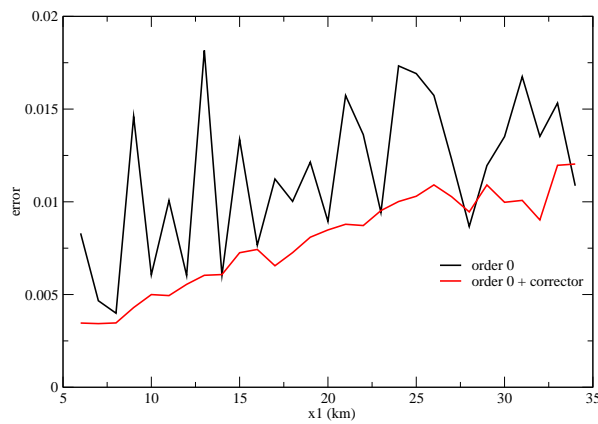


Figure 15. Error for the order 0 homogenized solution, $E_i(\dot{\mathbf{u}}^{\varepsilon_0,0})$, (black line) and for the order 0 homogenized solution plus first order corrector, $E_i(\dot{\mathbf{u}}^{\varepsilon_0,1/2})$, (red line) for receivers 5 to 35 (see Fig. 3) plotted as a function of their location along the x_1 axis and for $\varepsilon_0 = 0.15$.

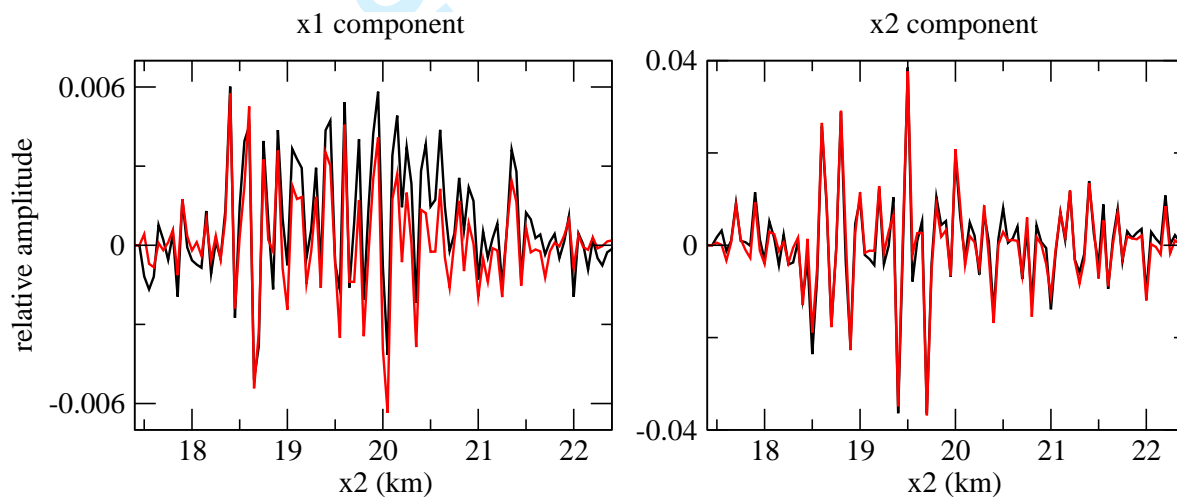


Figure 16. Cut along the line CD (see Fig. 3) for $\dot{\mathbf{u}}^{ref} - \dot{\mathbf{u}}^{\varepsilon_0,0}$ (black line) and for $\dot{\mathbf{u}}^{\varepsilon_0,1/2} - \dot{\mathbf{u}}^{\varepsilon_0,0}$ (red line) at $t = 5.5s$. On the left graph is plotted the x_1 component normalized by the maximum of $\dot{u}_{1,ref}$ and on right graph the x_2 component normalized by the maximum of $\dot{u}_{2,ref}$.

the 100m long of the edge of a random element. To investigate more closely the first order correction effect, in Fig. 16 is plotted the first order correction $\dot{\mathbf{u}}^{\varepsilon_0,1/2} - \dot{\mathbf{u}}^{\varepsilon_0,0}$ along the line CD (see Fig. 3) for $t = 5.5 s$, and compared to $\dot{\mathbf{u}}^{ref} - \dot{\mathbf{u}}^{\varepsilon_0,0}$. It appears that the fast oscillations are the same for both curves. The remaining differences are due to un-computed higher order asymptotic terms.

Finally, in Fig. 17 is shown the leading order moment tensor correction (45) effect for the source B. It can be seen that the moment tensor correction and the order 0 homogenized model allow to correctly reproduce the observed strong S wave with the correct time arrivals as well as the full waveform.

In the above study, the random model was generated such that the density and the Lamé param-

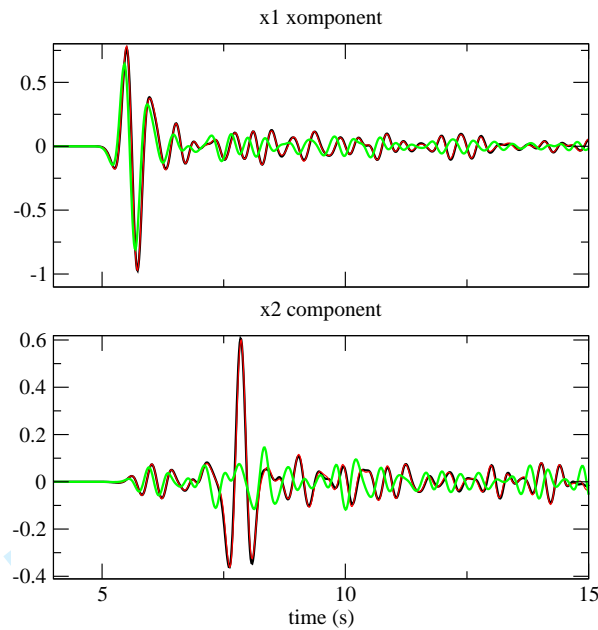


Figure 17. Velocity traces recorder at receiver 38 for source B. The reference solution (black line) is compared to the elastic filtering upscaling solution (green line) and to the order 0 homogenized solution with moment tensor correction (45) (red line).

ters were uncorrelated. Other tests were realized using other kinds of correlations between parameters and they all give similar results. We nevertheless show here the result when only the density varies randomly, the P and S waves velocities being kept constant in the whole domain. This case is interesting because it is known as a difficult case for another upscaling method developed by Gold *et al.* (2000). For our approach, such a case presents no specific difficulty as it can be seen in Fig. 18.

4.2 Marmousi2 model example

The same homogenization procedure is applied to the Marmousi2 model described in section 2.4.2. The spatial filter is the same as the one used in section 2.4.2, which, due to the change in velocities with depth (and then of the minimum wavelengths), implies an evolution of the values of the ε_0 parameter from 2 at the top of the model to 0.3 at the bottom. This is a strong limitation of our filtering technique which doesn't allow to obtain a roughly constant value for ε_0 throughout the whole domain. This is an aspect that should be investigated in a future work and a filtering based on wavelet decomposition, then allowing to adapt locally the cutoff of the filter, is probably an interesting lead to follow. In Fig. 19 are plotted the S velocity and the total anisotropy of the order 0 homogenized model. This smooth model allows to use a very simple mesh compared to the original mesh presented in Fig. 7. A sample of this mesh, with the homogenized S wave velocity in background, is presented in Fig. 20. As already mentioned in section 2.4.2, the simulations with such a simple mesh are much faster and it took only

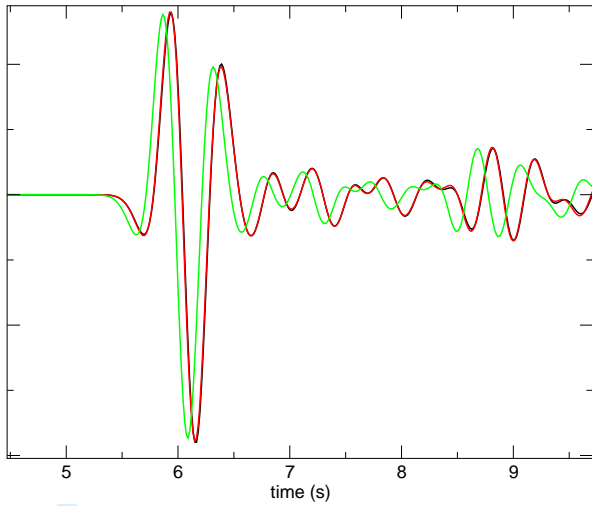


Figure 18. x_1 velocity component recorded at receiver 22 and source A (see Fig. 3) computed using SEM in a model with randomly generated density variations but with constant P and S velocities (reference solution, black line), in the corresponding order 0 homogenized medium with $\varepsilon_0 = 0.6$ (red line) and in velocity averaged model still with $\varepsilon_0 = 0.6$ (green line). Note that for the velocity averaged model, only the density is low pass filtered with $\varepsilon_0 = 0.6$ as the wave velocities remain constant.

one hour to compute the homogenized solution compared to the seven days required to obtain the reference solution using the same computing power. Traces recorded at the receiver location shown in Fig. 8 are shown in Fig. 20. The traces obtained using the order 0 homogenized medium are more accurate than the velocity filtering solution based on the same spatial filter. The fact the results are not as spectacular here as for the square random model example are mainly due to the heterogeneity spectrum of the Marmoursi2 model which roughly decreases as $1/k$ (k being the wavenumber of heterogeneities), while it is almost flat in the case of the random square model. Unfortunately, we can not pursue the same convergence analysis as it was done for the random square model example, mainly because of the presence of absorbing boundary conditions. Indeed, the Perfectly Matched Layers we are using (Festa & Vilotte, 2005) are not adapted to take anisotropy into account. Therefore, the anisotropy created by the homogenization at the domain boundaries is an issue that prevents to lead a precise convergence analysis as the one done for the random square example. Nevertheless, the result are good enough to show the interest of the procedure in such a case.

5 CONCLUSIONS AND PERSPECTIVES

We have presented a two scale homogenization procedure which can be applied to the upscaling process in non-periodic media. The critical point of this procedure is the practical construction of the fast (microscopic) part of the density and elastic tensor $\mathbf{c}^{\varepsilon_0}(\mathbf{x}, \mathbf{y})$ implied in well-known classical homog-

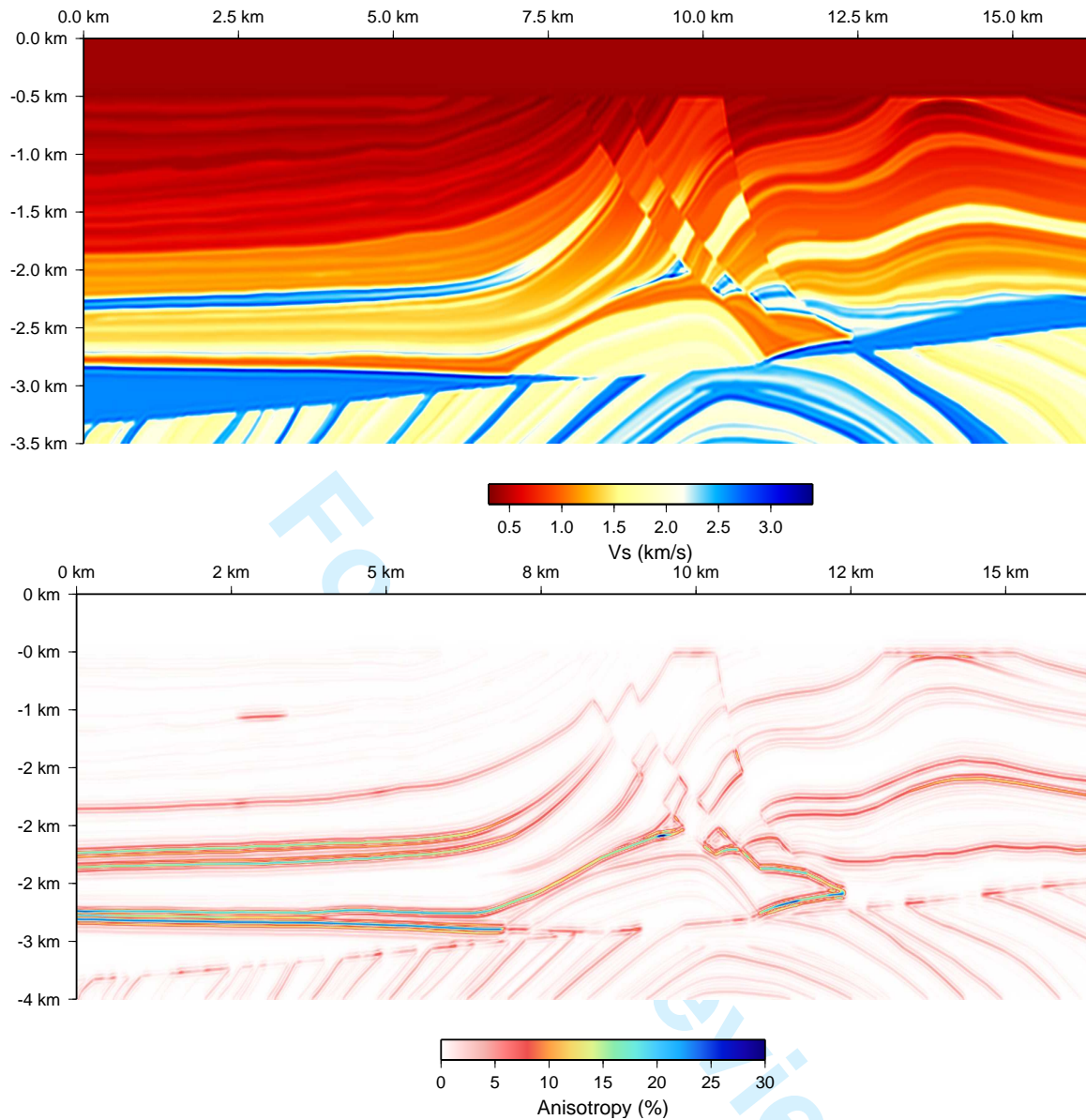


Figure 19. Order 0 Marmousi2 homogenized model for $\lambda_0 = 50$ m. Top graph: S velocity ($\sqrt{c_{2222}^*/\rho^*}$) Bottom graph: total anisotropy as defined Fig. 11.

enization procedures (in periodic media). Once this is done, the homogenization expansion is very similar to the one of classical two scale periodic homogenization. In the general case, it is not possible to go beyond the calculation of the leading order of the expansion, and that of the first order corrector. This nevertheless allows to find an effective medium to any general elastic medium with fast variations in all spatial directions. It also allows to retrieve the leading order corrector to a moment tensor source type as well as the first order correction at a receiver location, and then to take into account local structure effects. The study of two examples in this article, the random model, as well as the marmousi2 geological model, demonstrates the efficiency and accuracy of the method. This is an important step

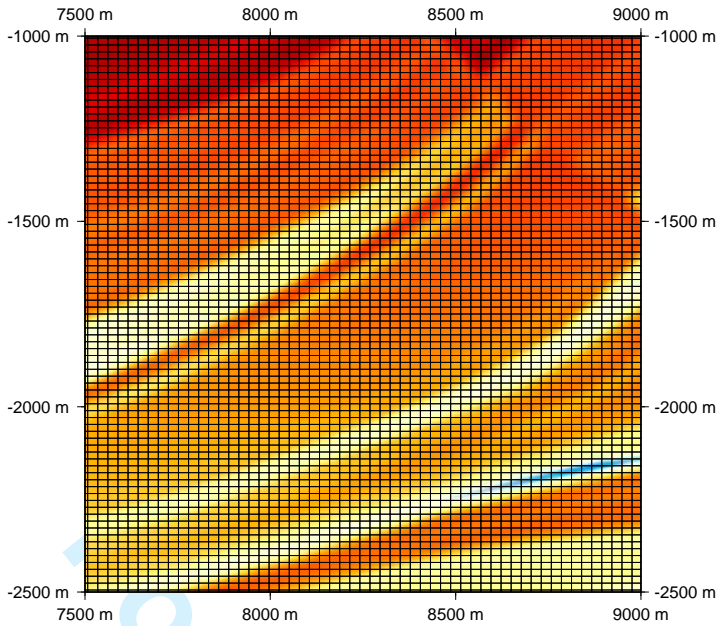


Figure 20. Sample of the spectral element mesh (black lines) used to solve the wave equation with the order 0 homogenized Marmousi2 model . The background color is the corresponding order 0 homogenized S velocity with the same color code as for Fig. 19.

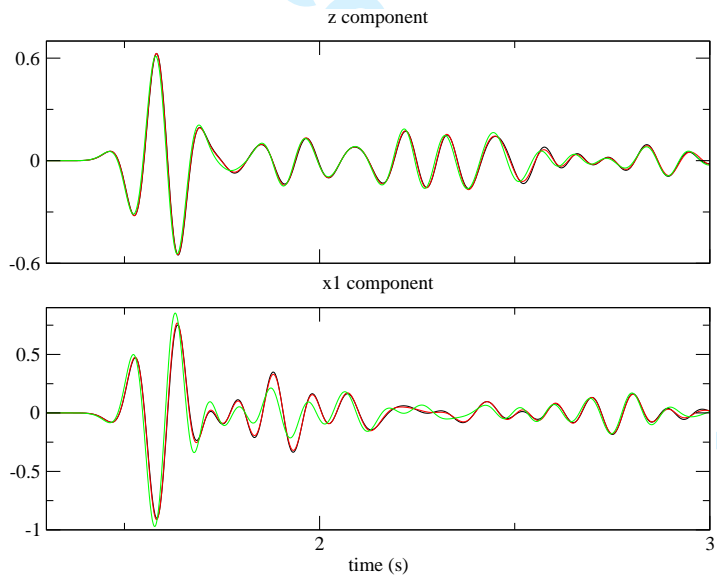


Figure 21. Velocity traces recorder at receiver 48. The reference solution (black line) is compared to the velocity filtering upscaled model (green line) and to the order 0 homogenized solution (red line). Both vertical (top graph) and horizontal (bottom graph) components are shown .

forward since the results of Backus (1962), which are applicable to non-periodic but layered media, and compared to the classical two scale homogenization theory, which is applicable to media showing fast variations in their physical properties in higher spatial dimensions, but only in the periodic case.

As already mentioned when studying wave propagation throughout the marmousi2 model, the spatially-constant, low pass filtering we used, may not be appropriate when applied to media where strong variations in the heterogeneity spectrum, arise. Other kinds of filtering, like ones involving wavelets for instance, may be more pertinent - and this will be the topic of a future work. The issue of boundary conditions in an homogenization procedure hasn't been treated in this article. It will be important to tackle this problem in a future work as it is known that the boundary conditions are important for surface waves and that the subsurface structures strongly influence waveforms (Capdeville & Marigo, 2007; Capdeville & Marigo, 2008).

The practical extension to 3D is obviously a priority. It should nevertheless not be a problem as the theoretical difficulties were faced when going from 1D to 2D and that no specific difficulty from 2D to 3D is expected.

The range of applications of such a development seems wide. One of them is the waveform modeling in complex media: for a given medium being able to upscale its properties to the wanted scale (knowing the corner frequency of the source) and to use the leading order effective medium $(\rho^{\varepsilon_0,*}, \mathbf{c}^{\varepsilon_0,*})$ in the favorite wave equation solver of a user, like finite differences or the Spectral Element Method, is an important alternative to the classical complex, and often impossible, meshing of the original medium. Note that, if the difficulty of the meshing for the forward problem and its consequences on the numerical cost can be avoided when using a homogenized model, the design of a mesh (or of multiple small meshes) for the homogenized problem itself can not be avoided. Nevertheless, the design of this mesh can be based on tetrahedron elements (even if the wave equation solver is based on a hexahedral mesh), the mesh sampling is independent on the frequency cutoff of the seismic sources that will be used and this, or these, meshes will be used only once for a given elastic model.

Another application is related to the study of the time arrival of the ballistic phase, in seismic exploration or geophysical imaging. It is known that this time arrival is only sensitive to a very smooth version of the real medium. A natural question is therefore: is this smooth medium the elastic model $(\rho^{\varepsilon_0,*}, \mathbf{c}^{\varepsilon_0,*})$ for a large ε_0 ? Fig. 13 seems to suggest it, but this should be studied more deeply as it is probably not the case.

Using our homogenization procedure for applications to the inverse problems is also in sight. A major and well-known result of our work is that microscopically (with respect to the wavefield) isotropic media, are macroscopically fully anisotropic, and this should be taken into account in tomographic studies for instance. Moreover, when inverting full waveforms, it may also not be a very good

idea to track for interfaces as they are homogenized (that means, smoothed) by the wavefield anyway. Finally, let us notice that this development gives the opportunity to build a multi-scale parametrization for the elastic properties and a well posed parametrization to take into account local effects on sources and receivers, of the inverse problem.

Some applications to other fields but with similar equations, like the stress loading of a complex geological structure, could also be considered.

A patent (Capdeville, 2009) has been filed on the non-periodic homogenization process by the "Centre national de la recherche scientifique" (CNRS) (this is by no mean a restriction to any academic research on the subject).

6 ACKNOWLEDGMENTS

Gaetano's SEM code. IDRIS IPGP clusters.

REFERENCES

Allaire, G. & Conca, C., 1998. Boundary layers in the homogenization of a spectral problem in fluid–solid structures. *SIAM J. Math. Anal.* 29(2), 343–379.

Allaire, G., Palombaro, M. & Rauch, J., 2009. Diffractive behavior of the wave equation in periodic media: weak convergence analysis. *Annali di Matematica*, **188**, 561–589.

Auriault, J. & Bonnet, G., 1985. Dynamique des composites élastiques périodiques. *Arch. Mech* 37(4-5), 269–284.

Backus, G., 1962. Long-wave elastic anisotropy produced by horizontal layering. *J. Geophys. Res.* 67(11), 4427–4440.

Browaeys, J. T. & Chevrot, S., 2004. Decomposition of the elastic tensor and geophysical applications. *Geophys. J. Int.*, **159**, 667–678.

Capdeville, Y., 2009. Procédé de détermination d'un modèle élastique effectif. Brevet FR 09 57637, filed on the October 29th 2009.

Capdeville, Y., Guillot, L. & Marigo, J. J., 2010. 1-D non periodic homogenization for the wave equation. *Geophys. J. Int.*, **00**, 000–000. In revision.

Capdeville, Y. & Marigo, J. J., 2007. Second order homogenization of the elastic wave equation for non-periodic layered media. *Geophys. J. Int.*, **170**, 823–838.

Capdeville, Y. & Marigo, J. J., 2008. Shallow layer correction for spectral element like methods. *Geophys. J. Int.*, **172**, 1135–1150.

- Chaljub, E., Komatitsch, D., Capdeville, Y., Vilotte, J.-P., Valette, B. & Festa, G., 2007. Spectral element analysis in seismology. In R.-S. Wu & V. Maupin (Eds.), *Advances in Wave Propagation in Heterogeneous Media*, Volume 48 of *Advances in Geophysics Series*, pp. 365–419. Elsevier.
- Festa, G., Delavaud, E. & Vilotte, J.-P., 2005. Interaction between surface waves and absorbing boundaries for wave propagation in geological basins: 2D numerical simulations. *Geophys. Res. Lett.*, **32**, L20306.
- Festa, G. & Vilotte, J.-P., 2005. The newmark scheme as velocity-stress time-staggering: an efficient implementation for spectral element simulations of elastodynamics. *Geophys. J. Int.*, **161**, 789–812.
- Fish, J. & Chen, W., 2004. Space-time multiscale model for wave propagation in heterogeneous media. *Comp. Meth. Appl. Mech. Engng*, **193**, 4837–4856.
- Geuzaine, C. & Remacle, J.-F., 2009. Gmsh: a three-dimensional finite element mesh generator with built-in pre- and post-processing facilities. *Int. J. Num. Methods in Engrg.*, ??, accepted.
- Gold, N., Shapiro, S. A., Bojinski, S. & Müller, T. M., 2000. An approach to upscaling for seismic waves in statistically isotropic heterogeneous elastic media. *Geophysics* 65(2), 1837–1850.
- Grechka, V., 2003. Effective media: A forward modeling view. *Geophysics* 68(6), 2055–2062.
- Guillot, L., Capdeville, Y. & Marigo, J. J., 2010. 2-D non periodic homogenization for the SH wave equation. *Geophys. J. Int.*, **00**, 000–000. Submitted.
- Hashin, Z. & Shtrikman, S., 1963. A variational approach to the elastic behavior of multiphase materials. *J. Mech. Phys. Solids*, **11**, 127–140.
- Hill, R., 1965. A self-consistent mechanics of composit materials. *J. Mech. Phys. Solids*, **13**, 213–222.
- Komatitsch, D. & Tromp, J., 2002. Spectral-element simulations of global seismic wave propagation, part II: 3-D models, oceans, rotation, and gravity. *Geophys. J. Int.*, **150**, 303–318.
- Komatitsch, D. & Vilotte, J. P., 1998. The spectral element method: an effective tool to simulate the seismic response of 2D and 3D geological structures. *Bull. Seism. Soc. Am.*, **88**, 368–392.
- Lurie, K. A., 2009. On homogenization of activated laminates in 1D-space and time. *Z. Angew. Math. Mech.*, **4**, 333–340.
- Mainprice, D. G., Barruol, G. & Ben Ismail, W., 2000. The seismic anisotropy of the earth's mantle: From single crystal to polycrystal. In S.-I. Karato, A. Forte, R. Liebermann, G. Masters, & L. Stixrude (Eds.), *Earth's Deep Interior: Mineral Physics and Tomography From the Atomic scale to the Global scale*. Washington, D.C.: AGU monograph.
- Marchenko, V. A. & Khruslov, E. Y., 2005. *Homogenization of Partial Differential Equations*, Volume 46 of *Progress in Mathematical Physics*. Birkhäuser, Boston.

- Martin, G. S., 2004. The marmousi2 model, elastic synthetic data, and an analysis of imaging and AVO in a structurally complex environment. Master's thesis, University of Houston.
- Martin, G. S., Wiley, R. & Marfurt, K. J., 2006. Marmousi2: An elastic upgrade for Marmousi. *The Leading Edge*, **25**, 156–166.
- Mercerat, E. D., Vilotte, J. P. & Sánchez-Sesma, F. J., 2006. Triangular spectral element simulation of two-dimensional elastic wave propagation using unstructured triangular grids. *Geophys. J. Int.*, **166**, 679–698.
- Moskow, S. & Vogelius, M., 1997. First-order corrections to the homogenised eigenvalues of a periodic composite medium. a convergence proof. *Proc. Roy. Soc. Edinburgh Sect. A* **127**(6), 1263–1299.
- Nguetseng, G., 2003. Homogenization structures and applications I. *Z. Anal. Anw.*, **22**, 73–107.
- Papanicolaou, G. C. & Varadhan, S., 1979. Boundary value problems with rapidly oscillating random coefficients. In *Proceedings of Conference on Random Fields, Esztergom, Hungary, 27, Seria Colloquia Mathematica Societatis Janos Bolyai*, pp. 835–873. North Holland, 1981.
- Pasquetti, R. & Rapetti, F., 2004. Spectral element methods on triangles and quadrilaterals: comparisons and applications. *J. Comp. Phys.*, **198**, 349–362.
- Priolo, E., Carcione, J. M. & Seriani, G., 1994. Numerical simulation of interface waves by high-order spectral modeling techniques. *J. Acoust. Soc. Am.*, **95**:2, 681–693.
- Rathod, H., abd B. Ventkatesudu, K. V. N. & Ramesh, N. L., 2004. Gauss legendre quadrature over a triangle. *J. Indian Inst. Sci.*, **84**, 183–188.
- Sanchez-Palencia, E., 1980. *Non homogeneous media and vibration theory*. Number 127 in Lecture Notes in Physics. Berlin: Springer.
- Shapiro, S. A., Schwarz, R. & Gold, N., 1996. The effect of random isotropic inhomogeneities on the phase velocity of seismic waves. *Geophys. J. Int.*, **123**, 783–794.
- Suquet, P., 1982. Plasticité et homogénéisation. Thèse d'Etat. Université Pierre et Marie Curie, Paris.
- Tiwary, D. K., Bayuk, I. O., Vikhorev, A. A. & Chesnokov., E. M., 2009. Comparison of seismic upscaling methods: From sonic to seismic. *Geophysics* **74**(2), wa3–wa14.
- Versteeg, R., 1994. The Marmousi experience: Velocity determination on a synthetic complex data set. *The Leading Edge*, **13**, 927–936.
- Willis, J. R., 1981. Variational principles for dynamic problems for inhomogeneous elastic media. *Wave Motion*, **3**, 1–11.

APPENDIX A:

Spatial low-pass filter design. To be able to separate the scales around λ_0 , we introduce a mother filter wavelet $w(\mathbf{x})$ such that its power spectrum is

$$\bar{w}(k) = \begin{cases} 1 & \text{for } k \leq a; \\ \frac{1}{2} \left(1 + \cos \left(\pi \frac{|k| - a}{b - a} \right) \right) & \text{for } |k| \in]a, b[; \\ 0 & \text{for } |k| \geq b. \end{cases} \quad (\text{A1})$$

where $k = |\mathbf{k}|$, a and b are two real around 1 defining the taper transition from 1 to 0 of the low pass filter. The space wavelet in the space domain is obtained with an Hankel transform:

$$w(\mathbf{x}) = \int_0^\infty \bar{w}(k) J_0(k|\mathbf{x}|) k dk, \quad (\text{A2})$$

where J_0 is the Bessel function of the first kind of order 0. Note that we have $\int_{\mathbb{R}^2} w(\mathbf{x}) d\mathbf{x} = 1$. We define $w_{k_0}(\mathbf{x}) = k_0 w(\mathbf{x}k_0)$ the same but contracted (if $k_0 > 1$) wavelet of corner spatial frequency k_0 . We still have $\int_{\mathbb{R}^2} w_{k_0}(\mathbf{x}) d\mathbf{x} = 1$. If $a = b = 1$, the low pass filter has a perfectly sharp cutoff for $k = k_0$. In that case the drawback is the space support of w_{k_0} is infinite and cannot be truncated with a good accuracy. A solution is to chose a smaller than 1 and b larger than 1 knowing that the largest $|b - a|$ is, the best a compact support for w_{k_0} is an accurate approximation. An example of such a wavelet is shown in Fig. 1.